



Tobias Achtsnit, BSc

Evaluating New Applications and Optimizing the Environmental Scanning Electron Microscope

MASTER'S THESIS

to achieve the university degree of

Diplom-Ingenieur

Master's degree programme: Technical Physics

submitted to

Graz University of Technology

Supervisor

Ao.Univ.-Prof. Dipl.-Ing. Dr.techn. Ferdinand Hofer

Co-Supervisor

Dipl.-Ing. Dr.techn. Johannes Rattenberger

Institute of Electron Microscopy and Nanoanalysis

Graz, February 2017

Affidavit

I declare that I have authored this thesis independently, that I have not used other than the declared sources/resources, and that I have explicitly indicated all material which has been quoted either literally or by content from the sources used. The text document uploaded to TUGRAZonline is identical to the present master's thesis.

Date

Signature

“The purpose of learning is growth, and our minds, unlike our bodies, can continue growing as long as we live.”

—Mortimer Adler

Acknowledgments

This thesis was conducted under the academic supervision of Prof. Ferdinand Hofer, head of the Institute of Electron Microscopy and Nanoanalysis and the Graz Centre for Electron Microscopy (FELMI-ZFE). I would like to thank Prof. Hofer for giving me the opportunity to work at FELMI-ZFE and to write my master's thesis in such a professional environment. I would especially like to thank Dr. Johannes Rattenberger, also at FELMI-ZFE, for his unconditional support during my entire research and his collegial supervision. His special dedication to electron microscopy, as well as his friendly manner, have made the time of my research very pleasant and his straight-forward approach to science was very impressive to me. In addition to that, I would like to thank the entire FELMI-ZFE staff for its loving manners and their willingness to help in all matters. I would like to thank Dr. Günther Krisper and Dr. Sylvia Schäffer from the Institute of Zoology at University of Graz who provided me with biological samples for my experiments several times. I would also like to thank Georg Weber who supported me in the measurement of the total scattering cross sections during his project lab.

I would especially like to thank all my good friends and companions who have made not only my time at the university, but also the time off university to a breathtaking and unforgettable experience. I could not have achieved this without your support. You were just great!

I honestly thank my family for the support and the warm welcome whenever I visited my home town after being away for longer times.

Lastly, I sincerely thank the Austrian Study Grant Authority for granting financial support during my entire study.

Table of Contents

Abstract	1
1 Introduction and Motivation	2
2 Fundamentals of Environmental Scanning Electron Microscopy	4
2.1 Introduction	4
2.2 Vacuum System	4
2.3 Primary Electron Beam Scattering	6
2.3.1 Scattering Cross Sections	6
2.4 Signal Detection	8
2.4.1 Secondary Electron Signal	8
2.4.2 Backscattered Electron Signal	10
2.5 ESEM Improvements	11
2.6 <i>In Situ</i> Studies of Fully Hydrated Samples	12
3 Optimized Working Distance for GSED	14
3.1 Introduction	14
3.2 Measurement Technique	15
3.2.1 Algorithm	15
3.2.2 Sample for SNR Determination	15
3.2.3 Error Estimation	17
3.3 Results	18
4 ESED versus Optimized GSED	25
4.1 Introduction	25
4.2 Design of ESED and Aperture Holder	25
4.3 Test Membrane	26
4.4 Implementation and Results	26
4.4.1 Wetting Experiment	29
5 Determination of Physical Constants: Total Scattering Cross Sections	32
5.1 Introduction	32
5.2 Measurement Technique	33
5.3 Results	35

5.3.1	Experimental Results	35
5.3.2	Interpretation of the Results	39
6	Purging and Biological Samples	41
6.1	Introduction	41
6.2	Purging Sequence	41
6.2.1	Measurement Technique	43
6.2.2	Results	44
6.3	Biological Samples	50
6.3.1	Liquid Biological Samples	50
6.3.2	Non-liquid Biological Samples	54
7	Conclusion	56
	Bibliography	58
	List of Figures	62
	List of Tables	69
	List of Abbreviations	70

Abstract

Previous work has shown that commercially available environmental scanning electron microscopes (ESEMs) operate far away from their physical limits. This work is based on a recently developed secondary electron detection system and an improved differential vacuum system. Through these systems image quality can be significantly improved at regions where the original design by the manufacturer fails. This improved ESEM setup was used for condensation experiments as well as for the determination of total scattering cross sections of water vapour in unprecedented accuracy. The purging sequence (purge-flood cycles), where the air in the sample chamber is replaced by water vapour for the purpose of analysing hydrated specimens, was accurately observed using an optical microscope camera inside the sample chamber. The purging sequence was significantly improved in order to minimize sample evaporation during pumpdown and an optimized purging procedure without technical changes to the microscope was introduced. These new prospects were used to observe liquid and non-liquid biological samples. Human blood cells without any sample preparation and tardigrades were imaged as well as live mites at high chamber pressure. The improved purging sequence in combination with the improved ESEM setup expands the field of ESEM applications up to new forms of *in situ* and *in vivo* studies which is of great interest for microscopy and life sciences.

1 Introduction and Motivation

In conventional scanning electron microscopes (CSEMs) specimens must be observed in high vacuum. This implicates several requirements on the specimen and limits the microscope's applications. In contrast, the environmental scanning electron microscope (ESEM) allows a gaseous environment in the sample chamber which enables to analyse electrically non-conductive and hydrated materials. Therefore, unprepared samples close to their natural conditions can be analysed. In addition to that the presence of gas atoms or molecules allows to expand the microscopic techniques. For example condensation and redox experiments as well as catalytic growth processes can be done and observed at microscopic level.

To perform this, the detection system and the vacuum system of an ESEM are different from a CSEM. First of all, a differential pumping system is necessary to enable a sufficient pressure gradient between the sample chamber and the electron column including the electron gun. This is implemented by two pressure limiting apertures (PLAs), which separate the sample chamber from the electron column (Lane, 1970; Robinson, 1975; Spivak *et al.*, 1977; Shah & Becket, 1979; Danilatos & Robinson, 1979).

Secondly, a significant component of an ESEM is the gaseous secondary electron detector (GSED). For signal amplification, the gas in the sample chamber is used (Danilatos, 1983, 1988, 1990b). Thiel *et al.* (1997) presented a model for the gas amplification effect and Fitzek (2014) has shown in his work that an improved SE-detector with—compared to the GSED—different shape and position provides much better image quality at high pressures (above 1000 Pa). In addition to that, previous work from Danilatos *et al.* (2000), Danilatos (2009), Danilatos *et al.* (2011) and Danilatos (2013b) has shown that the pressure limiting system used in commercial ESEMs operates far

away from physical limits. Based on these findings, Monte Carlo simulations and finite element simulations, the pressure limiting system was recently improved by Fitzek *et al.* (2016).

These improvements of SE detection and pressure limiting system provide the motivation for the present work. The first part basically deals with fundamentals of ESEM (chapter 2) and the analysis of the performance of the original ESEM setup using the GSED (chapter 3). In chapter 4 the improvements of SE detection and pressure limiting system are used for condensation experiments with previously unattained surface sensitivity. The determination of physical constants (total scattering cross sections) is also an important part of this work (chapter 5). Since life sciences are among the most important future research areas, the application of ESEM becomes more and more important. Finally, potential applications of the improved ESEM setup in this area (liquid and non-liquid biological samples) are investigated in chapter 6.

2 Fundamentals of Environmental Scanning Electron Microscopy

2.1 Introduction

This chapter should provide the necessary fundamentals to the characteristic features of an environmental scanning electron microscope, without any claim to completeness. The main focus is on topics which will be part of this work and the chapter also outlines the present knowledge as well as areas of development.

2.2 Vacuum System

In a CSEM the sample chamber and the electron column remain at high or ultra high vacuum which are typically between 10^{-1} Pa and 10^{-10} Pa. To prevent arcing, this pressure range has to be maintained in the column. In contrast to a CSEM, the sample chamber in an ESEM like the commercially available FEI Quanta series ESEMs can be maintained at pressures between 100 Pa to 4000 Pa depending on the imaging gas. This is achieved by a pressure limiting system consisting of two pressure limiting apertures (PLAs) combined with a differential pumping system. Figure 2.1 shows the vacuum system of an ESEM. The pressure gradient between the sample chamber and the gun is achieved by the PLAs and the differential pumping system (different vacuum levels). The elimination of the high vacuum in the sample chamber is the main advantage of the ESEM and allows analysis of non-conductive, vacuum intolerant, vacuum unfriendly and liquid samples close to their natural conditions. (Philips Electron Optics, 1996)

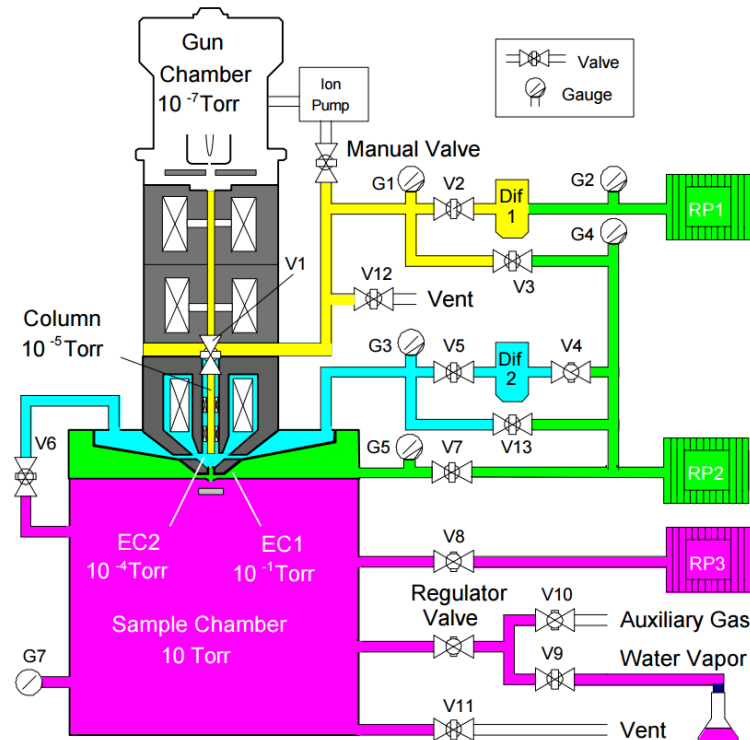


Figure 2.1: Schematic representation of the vacuum system of an ESEM. The vacuum system is divided into five stages with increasing vacuum from the bottom to the top level. The different stages are separated by pressure limiting apertures (PLAs). (Philips Electron Optics, 1996)

The essential part of the construction of the ESEM are the two PLAs at the bottom of the pole piece. The regions below, in between and above the PLAs are separately pumped and provide a large pressure difference in several orders of magnitude between the gun and the chamber. The PLAs are typically positioned in a removable aperture holder (FEI term: bullet). Figure 2.2 shows these PLAs and the different pressure levels. Depending on different configurations additional levels may be implemented. (Philips Electron Optics, 1996)

The sample chamber can be filled with different imaging gases via a special gas inlet. Typical imaging gases are water vapour, air, oxygen, argon or nitrogen because these gases are not toxic, non-corrosive and have good imaging properties (Danilatos, 1988).

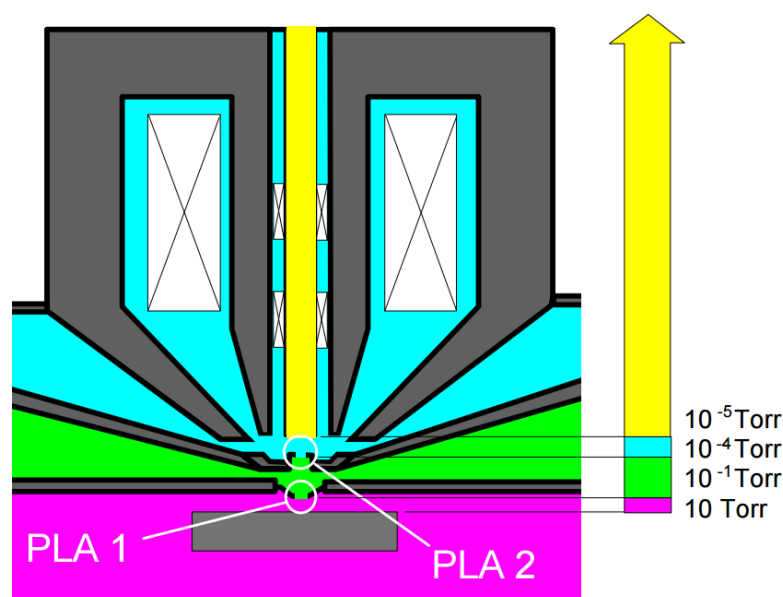


Figure 2.2: Enlarged pole piece from figure 2.1 showing two pressure limiting apertures (PLAs) which maintain high vacuum conditions in the electron column while there is comparatively high pressure in the sample chamber. (Philips Electron Optics, 1996)

2.3 Primary Electron Beam Scattering

Due to relatively high pressure of the gaseous environment in the sample chamber of an ESEM, the primary electron (PE) beam undergoes much more scattering events compared to the CSEM. The scattering of the PE beam is of particular importance for the achievable image quality and determines the signal-to-noise ratio (SNR). Hence, the usable signal is generated only by unscattered PEs and those electrons which are scattered out of the beam axis mainly produce background noise.

2.3.1 Scattering Cross Sections

After PEs pass the final PLA (PLA 1 in figure 2.2) they access the sample chamber and a certain percentage undergoes scattering with gas atoms or molecules. It is well known that the statistical distribution which describes this process is the Poisson dis-

tribution (events occur randomly) (Danilatos, 1988). The probability $P(x = 0)$ that a PE undergoes not a single scattering event can, therefore, be described as

$$P(x = 0) = e^{-m} \quad , \quad (2.1)$$

where x is the number of scattering events for a single electron and m is the average number of scattering events per electron (see figure 2.3 for schematic drawing of scattering influence of m). According to Danilatos (1990a) m is defined as

$$m = \frac{\sigma(U)}{k_B \cdot T} \cdot p \cdot \theta \quad , \quad (2.2)$$

where $\sigma(U)$ [m²] is the total scattering cross section for a specific accelerating voltage U [V], k_B [JK⁻¹] is the Boltzmann constant, T [K] is the temperature, p [Pa] is the pressure and θ [m] is the stagnation gas thickness which will be defined in the over next paragraph.

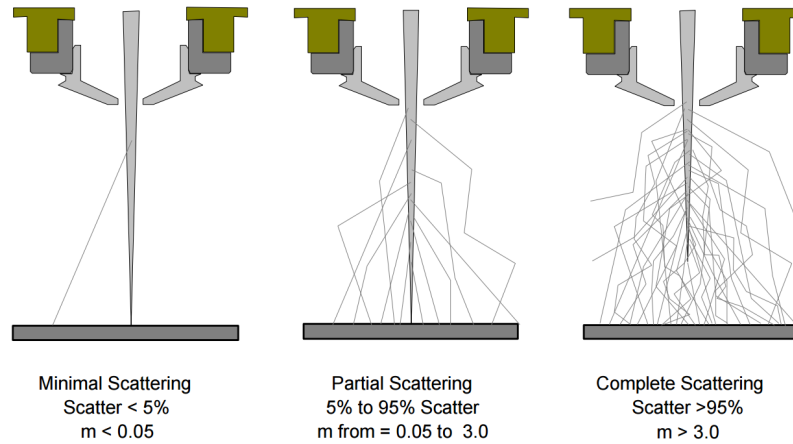


Figure 2.3: The average number of scattering events per electron m determines the scattering regimes. CSEMs operate in the minimal scattering regime, whereas ESEMs operate in the partial scattering regime. The complete scattering regime cannot be used for SEM imaging. (Philips Electron Optics, 1996)

Moreover, the fraction of PE beam I which is unscattered and reaches the sample surface is described by

$$I = I_0 \cdot e^{-m} = I_0 \cdot e^{-\frac{\sigma(U)}{k_B \cdot T} \cdot p \cdot \theta} \quad , \quad (2.3)$$

where I_0 [A] is the total beam current in high vacuum.

As already mentioned, there is a pressure gradient (several orders of magnitude difference in pressure) between the sample chamber and the electron column. Therefore, the stagnation gas thickness θ was introduced. θ describes the thickness of a gas layer at sample chamber pressure equivalent to the distance the beam travels through the gas and is defined as

$$\theta = \text{ED} + \Delta \quad , \quad (2.4)$$

where ED [m] is the environmental distance (distance between the final PLA (PLA 1) and the sample). Δ [m] is the additional stagnation gas thickness (simplification of the complex pressure behaviour above PLA 1 which assumes an immediate pressure decrease from sample chamber pressure to zero after a certain distance).

2.4 Signal Detection

2.4.1 Secondary Electron Signal

In CSEMs the mainly used SE detector is the Everhart-Thornley detector (ETD), but it cannot be used in presence of a gaseous environment because of electrical arching (ETD requires high electric field strength) (Goldstein *et al.*, 2003). Therefore, the gas itself is used for signal amplification by the gaseous secondary electron detector (GSED), which was introduced by Danilatos (1983), Danilatos (1988) and Danilatos (1990b).

The GSED from FEI company is situated at the bottom of the pole piece in form of a positively biased ring (a few hundred volts) whereby the primary electron beam travels through the center of the ring. Due to the electric field, the SEs which have typical

energies less than 50 eV are accelerated towards the detector. During their path to the detector, SEs undergo multiple collisions with present gas atoms or molecules and they can ionize them. The electrons coming from the ionization process get accelerated similarly and can ionize further gas atoms or molecules. The resulting electron cascade is nothing more than the amplification of the initial SE signal and can be collected by the GSED. The number of electrons generated in the electron cascade N [1] is described by

$$N = N_0 \cdot e^{\alpha \cdot d} \quad , \quad (2.5)$$

where N_0 [1] is the number of SEs leaving the sample surface, α [ion pairs/mm] is the first Townsend ionization coefficient and d [m] is the sample-detector distance (von Engel, 1965; Nasser, 1971). According to von Engel (1965) α is defined as

$$\alpha = A \cdot p \cdot e^{\frac{B \cdot p}{E}} \quad , \quad (2.6)$$

where E [V mm⁻¹] is the electric field strength between detector and the stage and A [mm⁻¹ torr⁻¹] and B [V mm⁻¹ torr⁻¹] are gas dependent constants.

The process of secondary electron signal amplification and the detection using the GSED is illustrated in figure 2.4. The PE beam usually accumulates negative charges at the surface of non-conductive samples (at least for typical CSEM electron energies) whereby the positive gas ions in the ESEM get attracted to the sample surface and recombine with these electrons (charge suppression) (Stokes, 2008). Hence, one of the main advantages of the present gaseous environment in the sample chamber is the possibility to analyse electrically non-conductive samples in the ESEM.

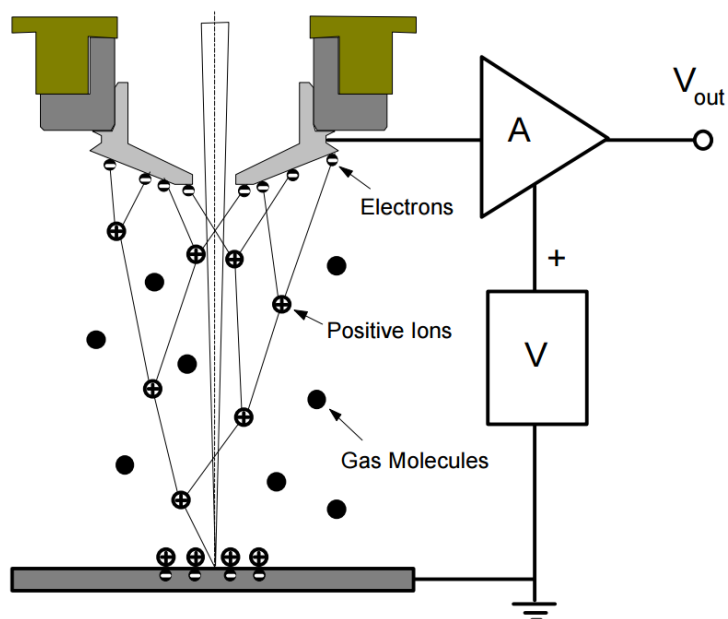


Figure 2.4: The positively biased gaseous secondary electron detector accelerates secondary electrons which in turn ionize gas atoms or molecules. The electrons coming from the ionization process themselves ionize further gas atoms and the result is an electron cascade, which is collected by the GSED. (Philips Electron Optics, 1996)

However, one must note that on the one hand the gas in the sample chamber enables signal amplification, but on the other hand comparatively high sample chamber pressure leads to PE beam scattering, which degrades image quality again.

2.4.2 Backscattered Electron Signal

Backscattered electrons (BSEs) leave the sample in an angular emission distribution with a maximum normal to the sample surface. Thus, the location of a BSE detector relative to the sample surface has strong influence on its detection efficiency (Goldstein *et al.*, 2003). Therefore, BSEs are usually detected at the bottom of the pole piece by a semiconductor detector. In use of a GSED, separate BSE detection is due to the position of the GSED not possible anymore, but the BSEs contribution degrades the collected SE signal (Philips Electron Optics, 1996).

2.5 ESEM Improvements

A schematic drawing of the pressure limiting system of the FEI Quanta line ESEMs can be seen in figure 2.5. As already mentioned, the GSED is positioned at the bottom of the pole piece. In this design, the final PLA (PLA 1) is given by the hole in the GSED ring which has a fixed diameter of $500\ \mu\text{m}$. The differential pumping system operates between PLA 1 and PLA 2 and the aperture holder has a cone shape.

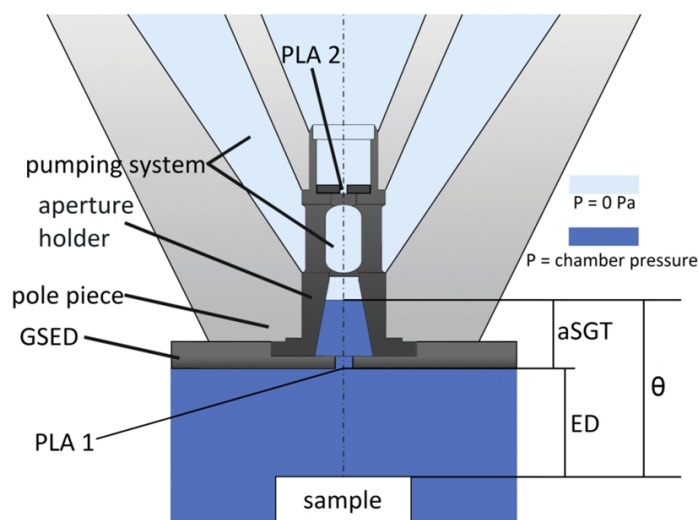


Figure 2.5: Schematic drawing of the pressure limiting system of the FEI Quanta line ESEMs. Image provided by FELMI-ZFE.

Recent work (Fitzek, 2014; Fitzek *et al.*, 2016) showed that ESEM image quality can be improved significantly by optimizing the pressure limiting system and the SE detection. A new aperture holder was presented by Fitzek *et al.* (2016) in order to reduce the additional stagnation gas thickness by changing the inner shape of the aperture holder and the PLAs (making them exchangeable). In addition to that, a newly designed experimental secondary electron detector (ESED) is placed on the sample table instead of GSED's position at the bottom of the pole piece. The ESED can have different shapes (needle, area, blade) (Fitzek, 2014). Positioning the SE detector on the sample table reduces the number of BSEs reaching the SE detector and allows BSE detection with the ordinary BSE detector simultaneously. The biggest advantage of this design is that

the sample-detector distance is independent of the ED. Figure 2.6 shows a schematic drawing of the improved pressure limiting system including the ESED according to the suggestions from Fitzek *et al.* (2016).

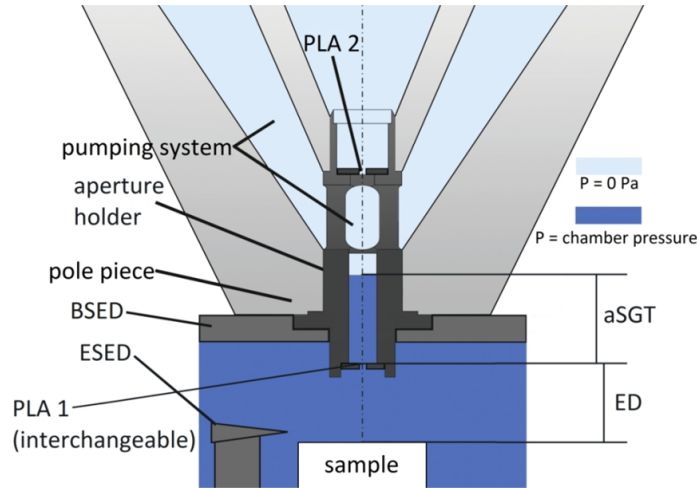


Figure 2.6: Schematic drawing of the improved pressure limiting system including the experimental secondary electron detector (ESED). Image provided by FELMI-ZFE.

In direct comparison to the original design (see figure 2.5) the improved design offers several advantages and provides the technical basis for this work.

2.6 *In Situ* Studies of Fully Hydrated Samples

The removal of water often changes the sample structure irreversibly and limits the spectrum of specimens which can be analysed in CSEM. Using water vapour as imaging gas in an ESEM in combination with a temperature-controlled stage (Peltier stage) allows analysing fully hydrated samples.

Figure 2.7 shows the vapour pressure diagram of water calculated by Antoine equation. By varying pressure and temperature any hydration state can be maintained and phase transitions can be studied as well.

In commercial ESEMs the state of saturated water vapour in the sample chamber is generated by several purge-flood cycles (purging). Purging decreases the pressure in

the sample chamber to a minimum value and afterwards floods the sample chamber with water vapour up to a defined value. This process is repeated several times until the sample chamber is filled with saturated water vapour.

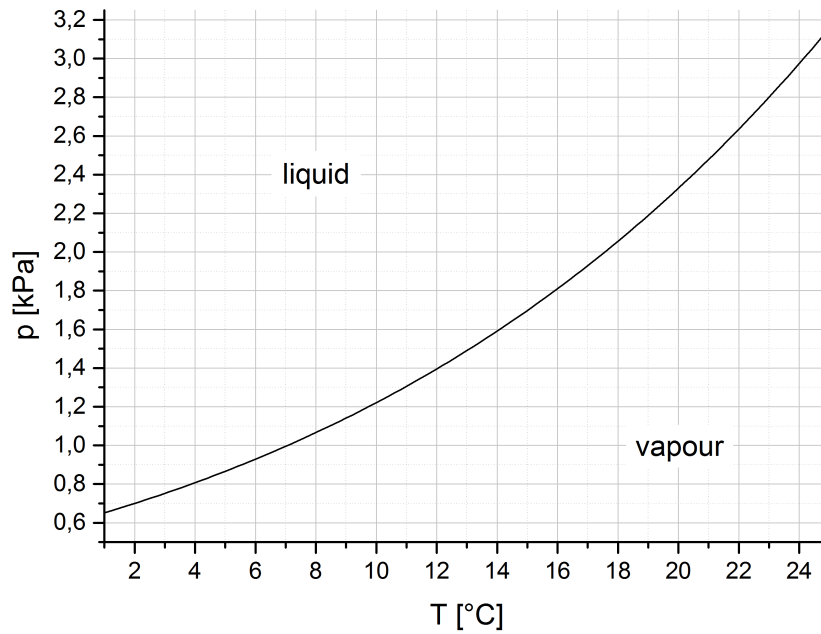


Figure 2.7: Vapour pressure diagram of water calculated by Antoine equation. By variation of pressure or temperature, the sample can be hydrated, evaporated or any hydration state can be maintained. Calculation parameters taken from Dortmund Data Bank (2017).

3 Optimized Working Distance for GSED

3.1 Introduction

Image quality in the ESEM mode is mainly influenced by the signal-to-noise ratio (SNR) and the SNR itself depends basically both on the length the PE beam travelling through the gas in the specimen chamber and on the SE signal amplification. By using the GSED from FEI company the two distances, namely the environmental distance (ED) and the amplification distance for SEs (distance between specimen and SE detector) are coupled (see figure 2.5 in section 2.5). Since a certain amount of gas is necessary to amplify the SE signal the ED, therefore, cannot always be kept as small as possible. Consequently, there must be a specific pressure-dependent ED which maximizes the SNR and therefore enables the best image quality.

In order to determine the optimized working distance (WD) for the GSED in the FEI Quanta 600 FEG ESEM[®], which is defined by the microscope as $WD [mm] = ED [mm] + 4.5 \text{ mm}$, a measurement technique described by Fitzek (2014) was used and an improved sample for this technique was produced.

3.2 Measurement Technique

3.2.1 Algorithm

The algorithm by Fitzek (2014) enables SNR determination by analysing images where there is dark background on one side and a bright object on the other side. The SNR is calculated by the algorithm using the logarithmic decibel scale

$$\text{SNR}_{\text{dB}} = 10 \cdot \log_{10} \frac{I_{\text{signal}}}{I_{\text{noise}}} \quad , \quad (3.1)$$

where I_{signal} is the difference according to amount between the average gray value of the bright area and the average gray value of the dark area. I_{noise} is estimated by a denoising routine and comparing the noiseless to the original image. The transition zone between dark and bright area in the picture is automatically excluded by the algorithm. (Fitzek, 2014)

3.2.2 Sample for SNR Determination

Initially, a sample according to Fitzek (2014) was used for test purposes. Figure 3.1a shows an SEM image of such a copper wire of approximately 12 μm diameter put on a carbon tape. It can be seen that the brightness distribution on the right side is clearly inhomogeneous and this comes basically from the cylindrical shape of the copper wire and the associated difference in height. For the algorithm, such a brightness distribution is not ideal and a more homogeneous sample is desirable.

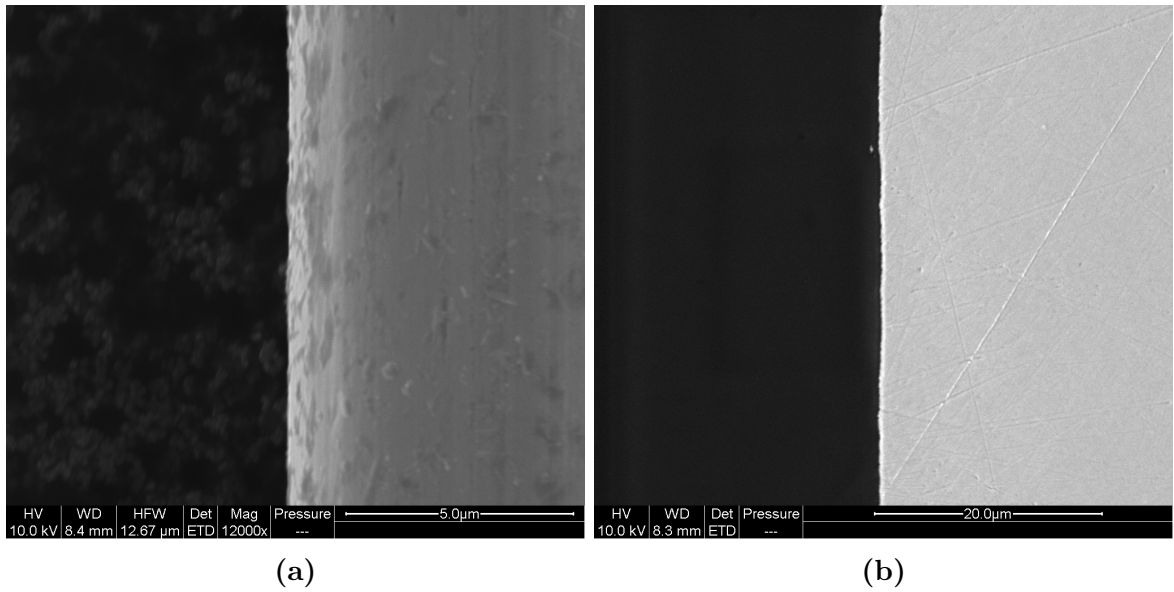


Figure 3.1: Design of a sample according to Fitzek (2014) **(a)**: approximately 12 μm copper wire put on carbon tape. Due to the cylindrical shape of the copper wire, clear differences in brightness can be seen on the right side. Improved design of sample **(b)** used for the SNR measurement in this work: copper block embedded in CaldoFix. Highly polished finally with diamond suspension down to 0.1 μm grain size.

Therefore, an improved sample was produced. Figure 3.1b shows an SEM image of a copper block embedded in CaldoFix¹. The surface was highly polished finally with diamond suspension down to 0.1 μm grain size. As it can be clearly seen there is no height difference between the dark and the bright area and therefore the brightness distribution in the bright area is much more homogeneous compared to the original design of the sample according to Fitzek (2014). Figure 3.2 shows the mean gray value of all lines from the original sample compared to the improved sample. The homogeneous brightness distribution in both areas is clearly visible for the improved sample. However, at the transition between dark and bright area, a very bright signal appears at the edge of the copper block. Since the algorithm excludes the transition zone, this edge effect does not influence the overall performance of the algorithm.

¹Hardener from Struers GmbH

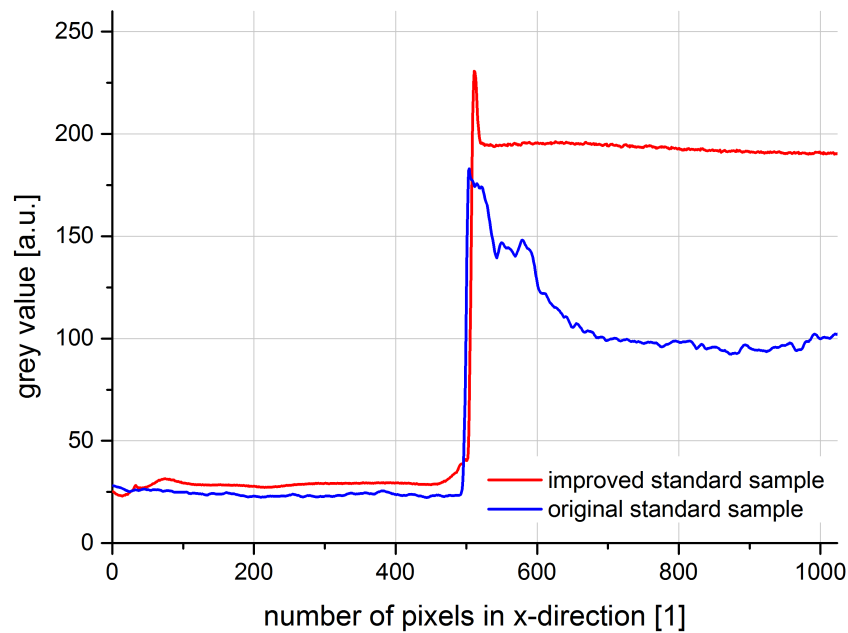


Figure 3.2: Average mean gray value (from 0 = black to 255 = white) of all lines from original sample compared to improved sample.

3.2.3 Error Estimation

In order to test the improved sample and estimate the error of the algorithm for the desired purposes the following measurement series was done: 10 images in ESEM mode (water vapour environment, pressure at 250 Pa, fixed WD at 10.0 mm and 20.0 kV accelerating voltage) were taken whilst focus, contrast and brightness settings were reset after each picture. Before starting the image acquisition the beam current was set to 1.0 nA in high vacuum once using a Faraday cup (see chapter 5.2).

Figure 3.3 shows the SNR of each image calculated by the algorithm. The average SNR is 19.79 dB with a standard deviation of 0.22 dB. Fitzek (2014) gives a value of 0.13 dB for the systematic error of the algorithm. Therefore, the overall error is assumed with a value of 0.40 dB.

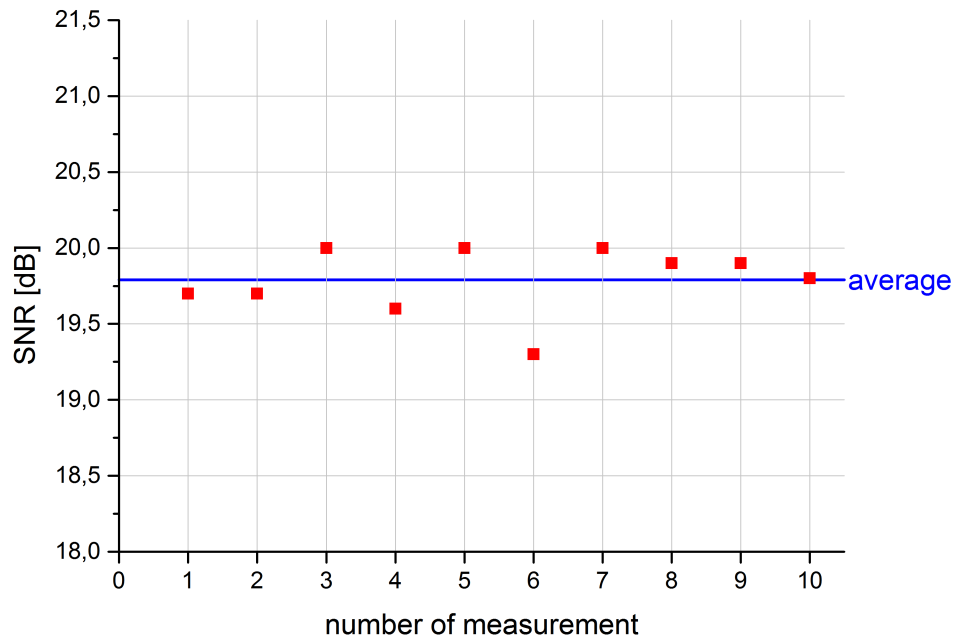


Figure 3.3: Error estimation of the used algorithm: SNR of 10 ESEM images using the GSED acquired under the same conditions (water vapour environment, pressure of 250 Pa, fixed WD of 10.0 mm, accelerating voltage of 20.0 kV and a beam current of 1.0 nA) calculated by the algorithm of Fitzek (2014).

3.3 Results

To determine the optimized WD for the GSED the SNR was measured at different pressures and accelerating voltages. Fitzek (2014) showed in his work that the beam current deviates in the first minutes after switching on the accelerating voltage and therefore recommends to wait at least 20 min to ensure constant beam current. After switching on the accelerating voltage and waiting the recommended time the beam current was always set to 1.0 nA using a Faraday cup in high vacuum mode and afterwards the mode was switched to ESEM (water vapour environment). All measurements were done on the FEI Quanta 600 FEG ESEM[®]. Figures 3.4, 3.5, 3.6, 3.7, 3.8 and 3.9 show the results for different accelerating voltages.

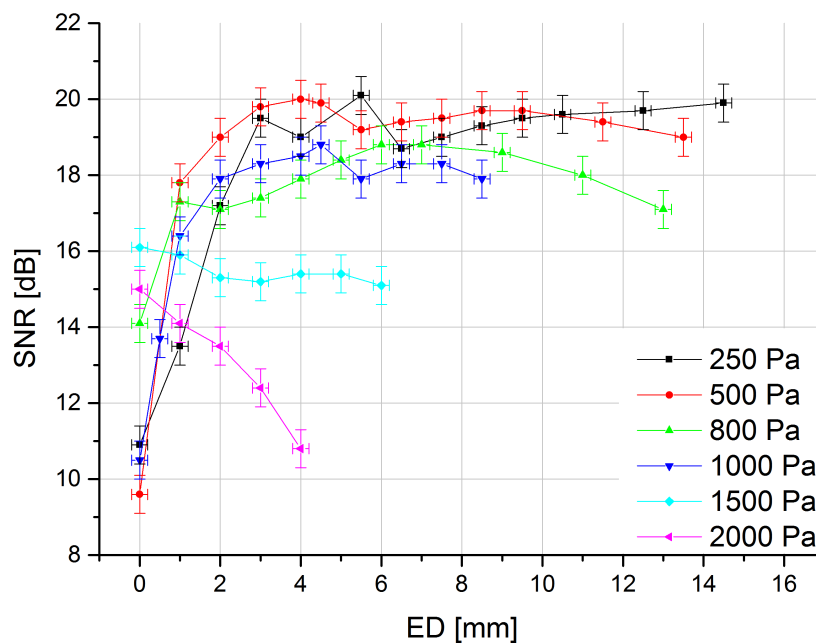


Figure 3.4: SNR as a function of the ED measured for different pressures at an accelerating voltage of 30.0 kV and a beam current of 1.0 nA.

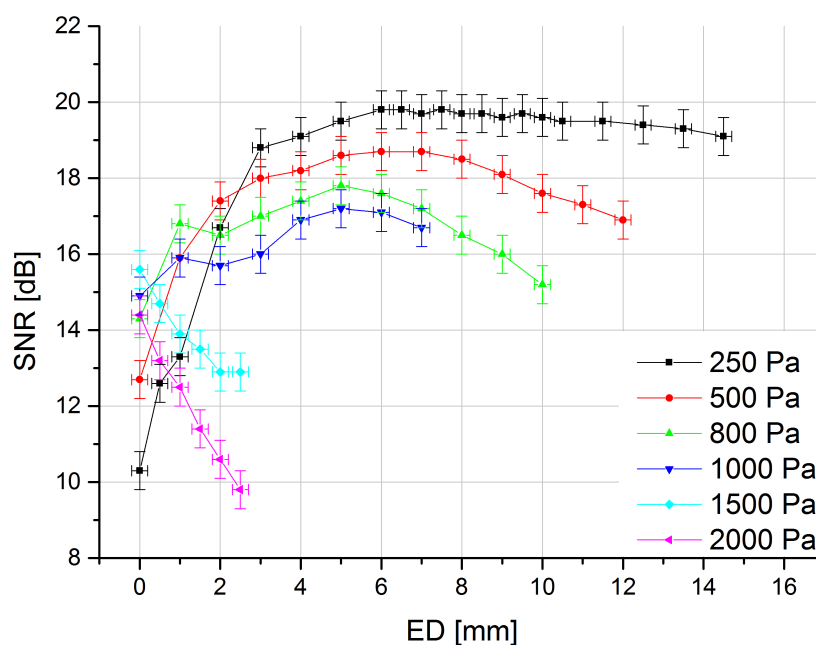


Figure 3.5: SNR as a function of the ED measured for different pressures at an accelerating voltage of 20.0 kV and a beam current of 1.0 nA.

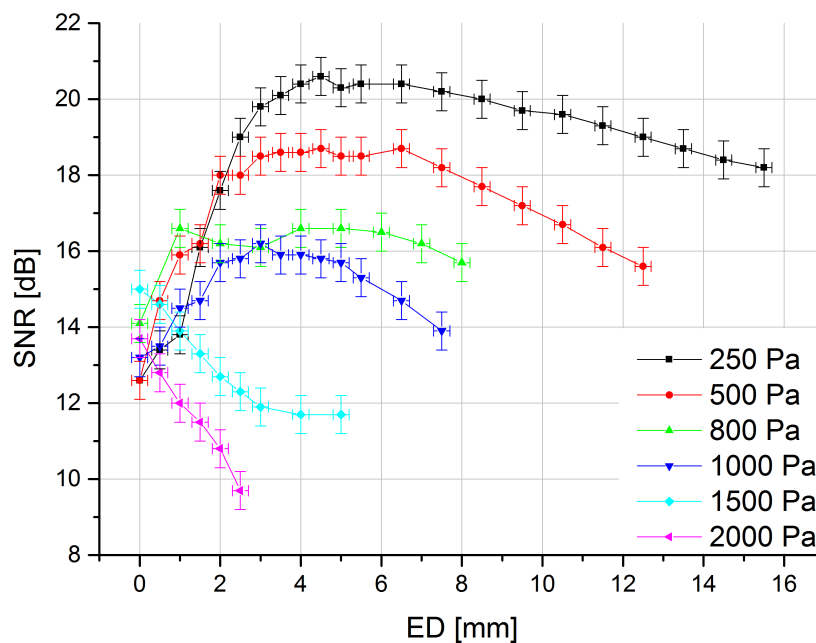


Figure 3.6: SNR as a function of the ED measured for different pressures at an accelerating voltage of 15.0 kV and a beam current of 1.0 nA.

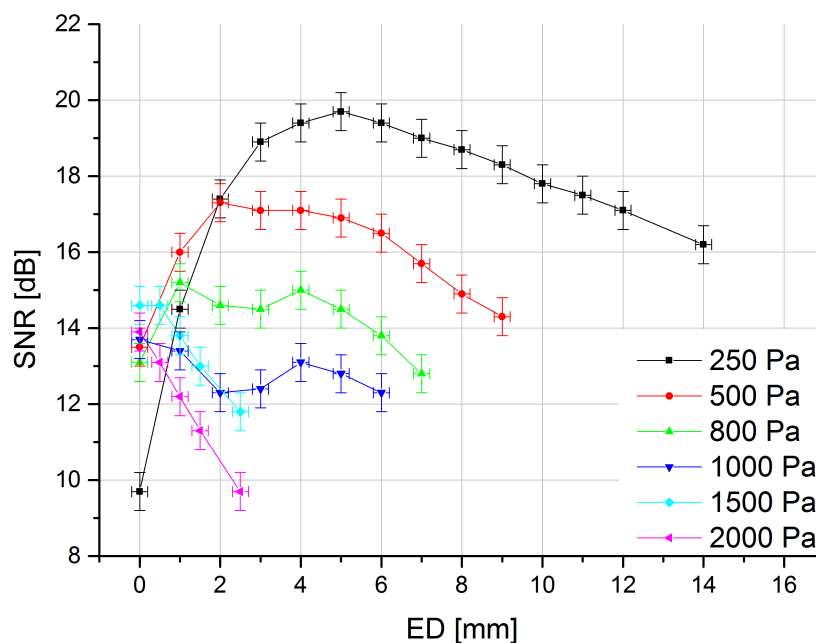


Figure 3.7: SNR as a function of the ED measured for different pressures at an accelerating voltage of 10.0 kV and a beam current of 1.0 nA.

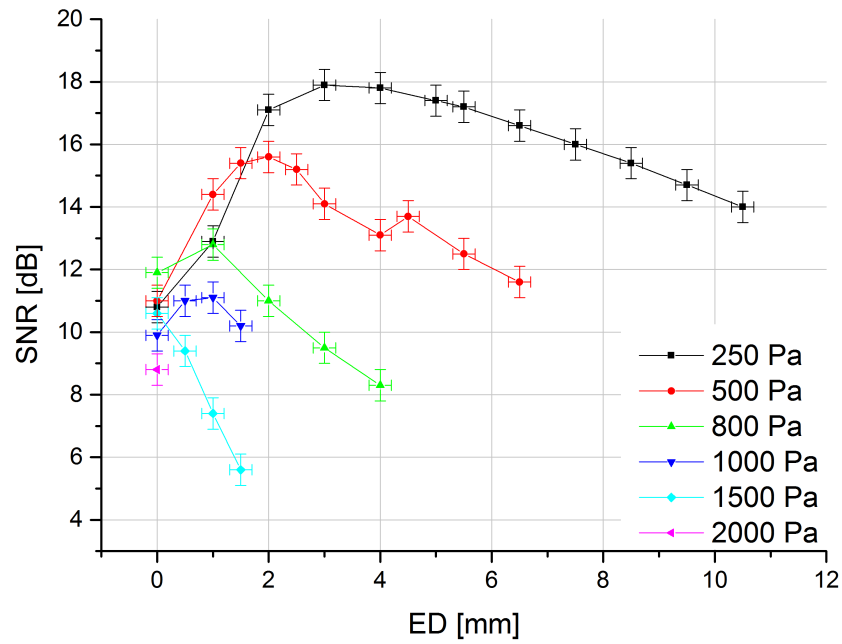


Figure 3.8: SNR as a function of the ED measured for different pressures at an accelerating voltage of 5.0 kV and a beam current of 1.0 nA.

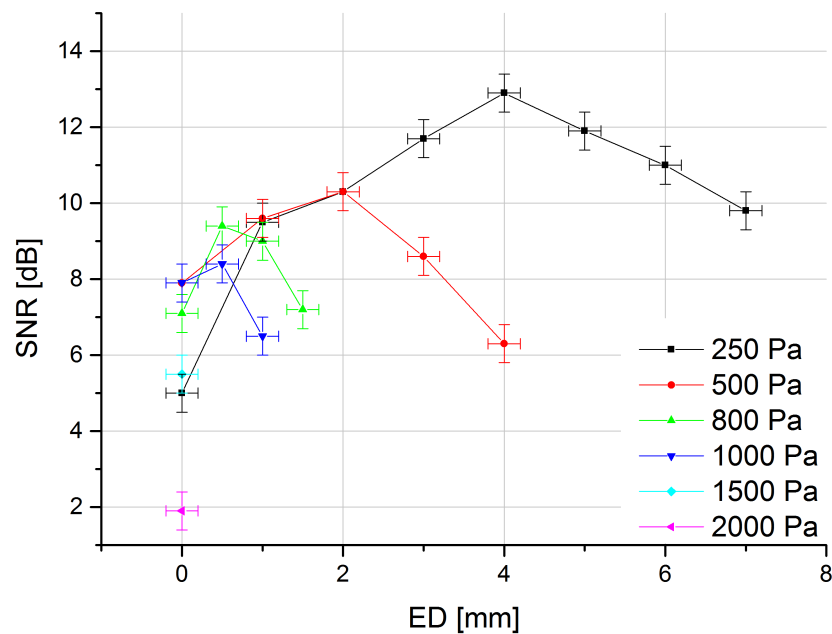


Figure 3.9: SNR as a function of the ED measured for different pressures at an accelerating voltage of 3.0 kV and a beam current of 1.0 nA.

For an accelerating voltage of 30.0 kV, for pressures up to 1000 Pa and an ED above 3 mm the SNR basically reaches constant values over a wide ED range. Figure 3.4 shows this behaviour where there is no significant maximum of the SNR. For pressures higher than 1000 Pa the SNR becomes worse with increasing ED and the best SNR can be achieved by keeping the ED very small. Since the probability for the PE beam to undergo scattering is also dependent on the accelerating voltage (see equation (2.2)) a high accelerating voltage leads to a high SNR.

By decreasing the accelerating voltage the probability for scattering events gets higher and the SNR for different pressures shows significant maxima at specific EDs (see figures 3.5, 3.6 and 3.7 for accelerating voltages of 20.0 kV, 15.0 kV and 10.0 kV). These figures show clearly that up to a pressure of 1000 Pa the choice of optimal ED has significant influence on SNR and in consequence directly on the maximum achievable image quality. For low accelerating voltages (see figures 3.8 and 3.9 for accelerating voltages of 5.0 kV and 3.0 kV) the achievable SNR decreases continuously and the optimal ED moves towards minimum possible distance ($ED \approx 0.0$ mm which equals $WD \approx 4.5$ mm).

For each graph of figures 3.4, 3.5, 3.6, 3.7, 3.8 and 3.9 the ED with maximum SNR ED_{opt} was estimated and due to practical reasons converted to $WD_{opt} = ED_{opt} + 4.5$ mm. The resulting graphs can be found in figure 3.10. From this plot, it can be seen that WD_{opt} strongly depends both on the accelerating voltage and on the pressure. Up to a pressure of approximately 1000 Pa, a certain WD is useful to achieve the best SNR. Above 1500 Pa the probability of PE beam scattering becomes extremely high. Increasing the WD then decreases the SNR which means that scattering is the limiting process and SE amplification is no longer significant. Taking all these measurement results into consideration, it can be said that the performance of the GSED strongly depends on both, the accelerating voltage and the chamber pressure.

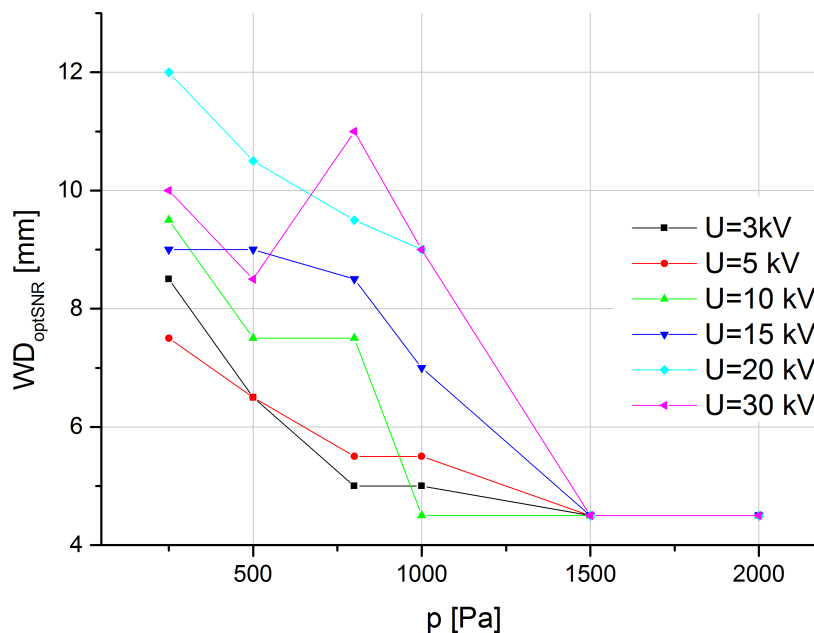


Figure 3.10: Optimized working distance WD_{opt} as a function of pressure for different accelerating voltages.

In summary, the GSED of the FEI Quanta 600 FEG ESEM[®] performs well at pressures below 1000 Pa using accelerating voltages above approximately 5 kV. Since this covers only a small part of the ESEM range (e.g. up to 2700 Pa for water vapour), the GSED covers basically only low pressure and high voltage applications. An improved detector design such as that described in section 2.5 is, therefore, desirable for applications beyond the performance of the GSED.

Finally, for practical purposes, the ranges of WD_{opt} are summarized numerically under consideration of the experimental and the systematic error of the used method in table 3.1.

Table 3.1: Results of measurement for optimized working distance WD_{opt} for different pressures and accelerating voltages. The values give the range where the maximum SNR was measured within the experimental and systematic error of the method.

p [Pa]	WD_{opt} [mm] at accelerating voltage of					
	3.0 kV	5.0 kV	10.0 kV	15.0 kV	20.0 kV	30.0 kV
250	8.5	6.5–10.0	7.5–11.5	7.0–13.0	8.5–18.0	> 7.5
500	5.5–6.5	6.0–7.0	6.5–10.5	6.5–13.0	7.0–13.5	6.5–16.0
800	5.0–5.5	< 5.5	5.5–9.5	5.5–11.5	7.0–11.5	8.5–15.5
1000	≤ 5.0	≤ 5.5	≤ 5.5	6.5–10.0	8.5–11.5	7.5–12.0
1500	4.5	4.5	≤ 5.5	≤ 5.0	≤ 5.0	< 6.5
2000	4.5	4.5	≤ 5.0	≤ 5.0	4.5	≤ 5.5

4 ESED versus Optimized GSED

4.1 Introduction

The previous chapter showed that the original GSED of FEI company enables good image quality under relatively low pressure (up to 1000 Pa) and high accelerating voltage (above 5 kV) conditions. Since this covers only a small part of the ESEM pressure range (e.g. pressures up to 2700 Pa for water vapour) and some samples are very sensitive concerning irradiation with electrons (Egerton *et al.*, 2004), an experimental secondary electron detector (ESED) in combination with an improved aperture holder was tested regarding image quality and directly compared to the performance of the original microscope configuration (GSED and original aperture holder).

4.2 Design of ESED and Aperture Holder

As already described in section 2.5, a new aperture holder with exchangeable PLAs was designed at the Institute of Electron Microscopy and Nanoanalysis and Graz Centre for Electron Microscopy (FELMI-ZFE) (patent pending from Rattenberger *et al.*, 2014). The new aperture holder improves the performance of FEI Quanta line ESEMs considerably (Fitzek *et al.*, 2016). Furthermore, it was showed that changing the shape and position of the SE detector (see figure 2.6 in section 2.5) also yields to appreciable improvements especially at comparatively high pressures. In this work, a tungsten needle tip fixed on the sample table was used for SE detection. Therefore, a special Teflon holder was produced which enables accurate positioning of the needle tip, protection against slipping and provides electrical insulation between the needle tip and the rest

of the microscope.

4.3 Test Membrane

MicroPES[®] 2F is a special polymer polyethersulfone membrane for microfiltration of fluids and has a typical pore diameter of 0.2 μm . The membrane has pores with similar size and density on both surfaces, whereas the ‘air side’ has a slightly lower porosity compared to the ‘roll side’. (Ulbricht *et al.*, 2007)

4.4 Implementation and Results

By using a Peltier stage the MicroPES[®] 2F membrane was cooled to 4–5 °C inside the sample chamber of the FEI Quanta 600 FEG ESEM[®]. This temperature contributes to a water vapour pressure of approximately 800 Pa (see figure 2.7). The choice of these parameters is founded by the previous chapter 3 which showed clearly that the GSED operates best at pressures below 1000 Pa. Under these conditions wetting experiments can be performed easily since further cooling to 2–3 °C leads to a transition from the gaseous to the liquid phase of water (condensation).

Figure 4.1 shows an ESEM image of the membrane using the GSED and a PE beam energy of 7.0 keV. To ensure optimized imaging conditions the WD was set to 5.5 mm in accordance with table 3.1. It can be clearly seen that the electron beam penetrates the surface deeply and consequently deeper membrane layers become visible. Therefore, the energy of the PE beam has to be considerably decreased to enable surface-sensitive imaging.

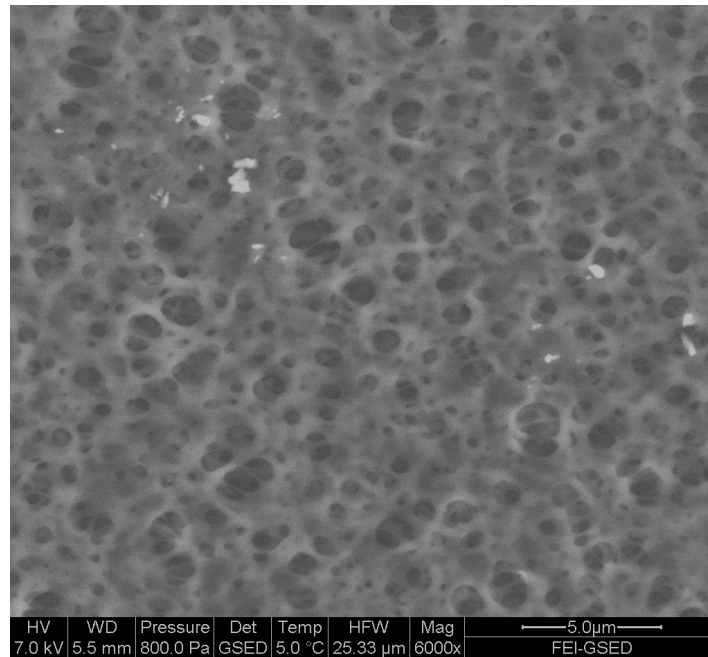


Figure 4.1: MicroPES[®] 2F membrane analysed with GSED. Pixel dimension: 1024x884; Dwell time: 1 μsec; Frame time: 0.97 sec.

As can be seen in figure 4.2 decreasing the energy of the PE beam makes image quality significantly worse. At a beam energy of 3.0 keV image quality is very poor and imaging with lower electron energies is hardly possible under these conditions.

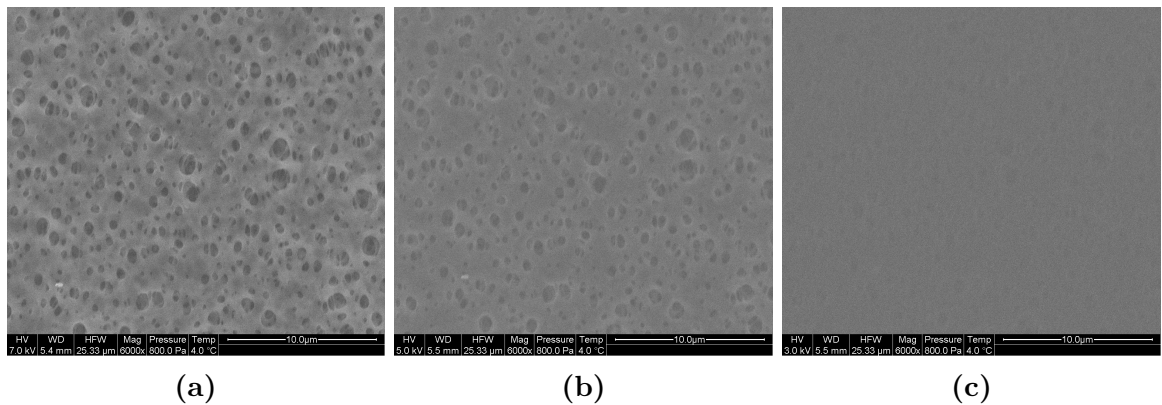


Figure 4.2: Performance of GSED in combination with original aperture holder at PE beam energies of 7.0 keV (a), 5.0 keV (b) and 3.0 keV (c). Image quality is strongly dependent on PE beam energy and very poor for low energies. Pixel dimension: 1024x884; Dwell time: 0.5 μsec; Frame time: 0.49 sec.

To test whether the image quality at low PE beam energies can be improved, the GSED was replaced by an ESED in form of a tungsten needle tip according to Fitzek (2014). In order to position the needle tip fixed on the sample table instead of the bottom of the pole piece, a Teflon holder was constructed. Figure 4.3 shows the holder fixed on the Peltier cooling stage and the position of the needle tip in relation to the sample surface. The original aperture holder was replaced by a modified design (Fitzek *et al.*, 2016) and a 200 μm aperture was installed as final PLA.

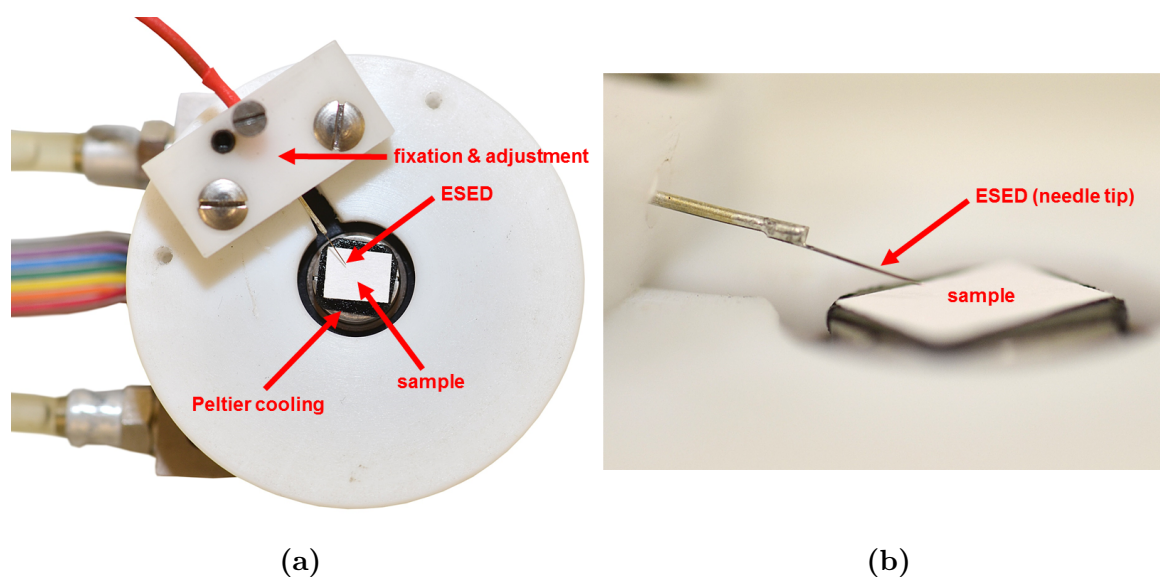


Figure 4.3: Positioning of ESED (tungsten needle tip) above sample. Teflon holder (a) (white) attached to the Peltier stage. The position and height of the needle can be adjusted using the screws. Position of needle tip (b) in direct proximity to the sample surface.

To compare the performance of the new setup to the original FEI setup three images were acquired under the same conditions as those in figure 4.2. The results can be found in figure 4.4. The images show a considerably improved image quality with the surface structure of the membrane being plainly visible even at a PE beam energy of 3.0 keV.

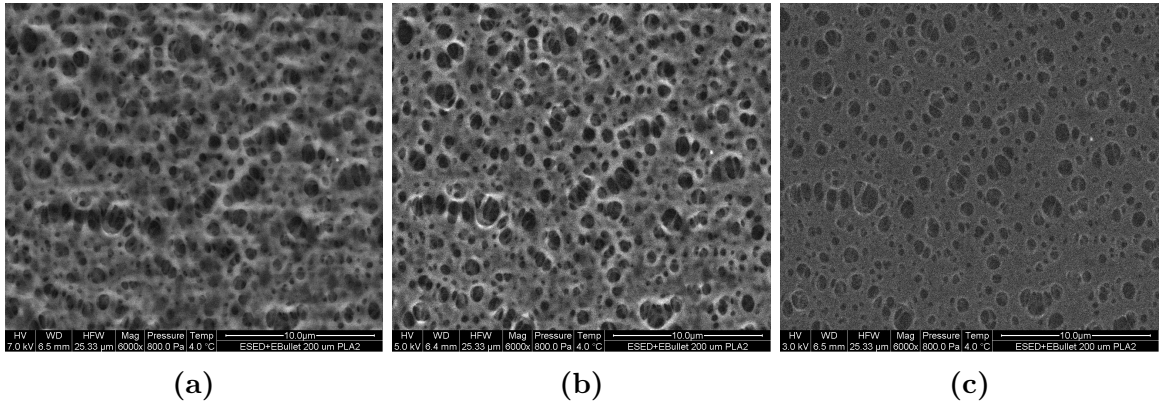


Figure 4.4: Performance of ESED (tungsten needle tip fixed on sample table) in combination with modified aperture holder (final PLA diameter of $200\ \mu\text{m}$) at PE beam energy of $7.0\ \text{keV}$ (a), $5.0\ \text{keV}$ (b) and $3.0\ \text{keV}$ (c). Image quality remains sufficiently well, even at low PE beam energies. Pixel dimension: 1024×884 ; Dwell time: $0.5\ \mu\text{s}$; Frame time: $0.49\ \text{sec}$.

4.4.1 Wetting Experiment

Because of the significant improvement in image quality by using the ESED in combination with the modified aperture holder wetting experiments with low PE beam energies can be performed. In order to demonstrate the possibilities of the new method two wetting experiments were done at PE beam energies at which the GSED is no longer performing sufficiently. Figure 4.5 shows wetting of the membrane during a cooling process starting at $2.9\ ^\circ\text{C}$ with a cooling rate of $0.2\ ^\circ\text{C}/\text{min}$ and PE beam energy of $5.0\ \text{keV}$. The dynamic process of the pores being filled continuously with water is clearly visible but the PE beam penetrates the surface in a way that deeper located layers are still visible.

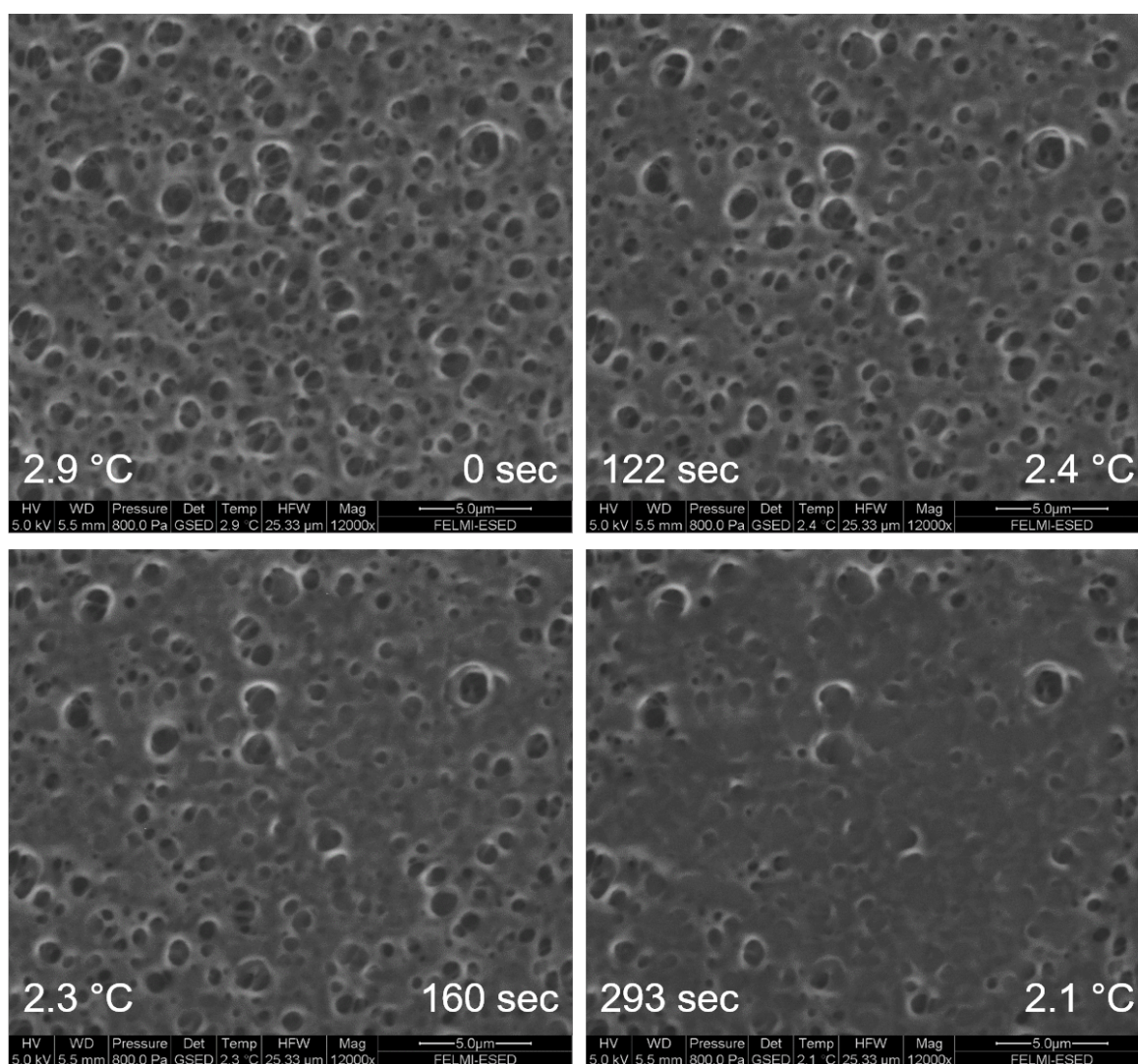


Figure 4.5: Wetting experiment with PE beam energy of 5.0 keV at 800 Pa. Membrane pores are continuously filled with water during cooling from 2.9 °C with a cooling rate of 0.2 °C/min. Pixel dimension: 1024x884; Dwell time: 10 μsec; Frame time: 9.48 sec.

In order to increase surface sensitivity, the PE beam energy was further decreased. Figure 4.6 shows wetting of the membrane during a cooling process starting at 4.0 °C with a cooling rate of 0.4 °C/min and a PE beam energy of 3.0 keV. In this experiment, a sufficient increase of surface sensitivity could be achieved and the images basically show only the top layer of the membrane. The dynamic formation of droplets on the surface is clearly visible.

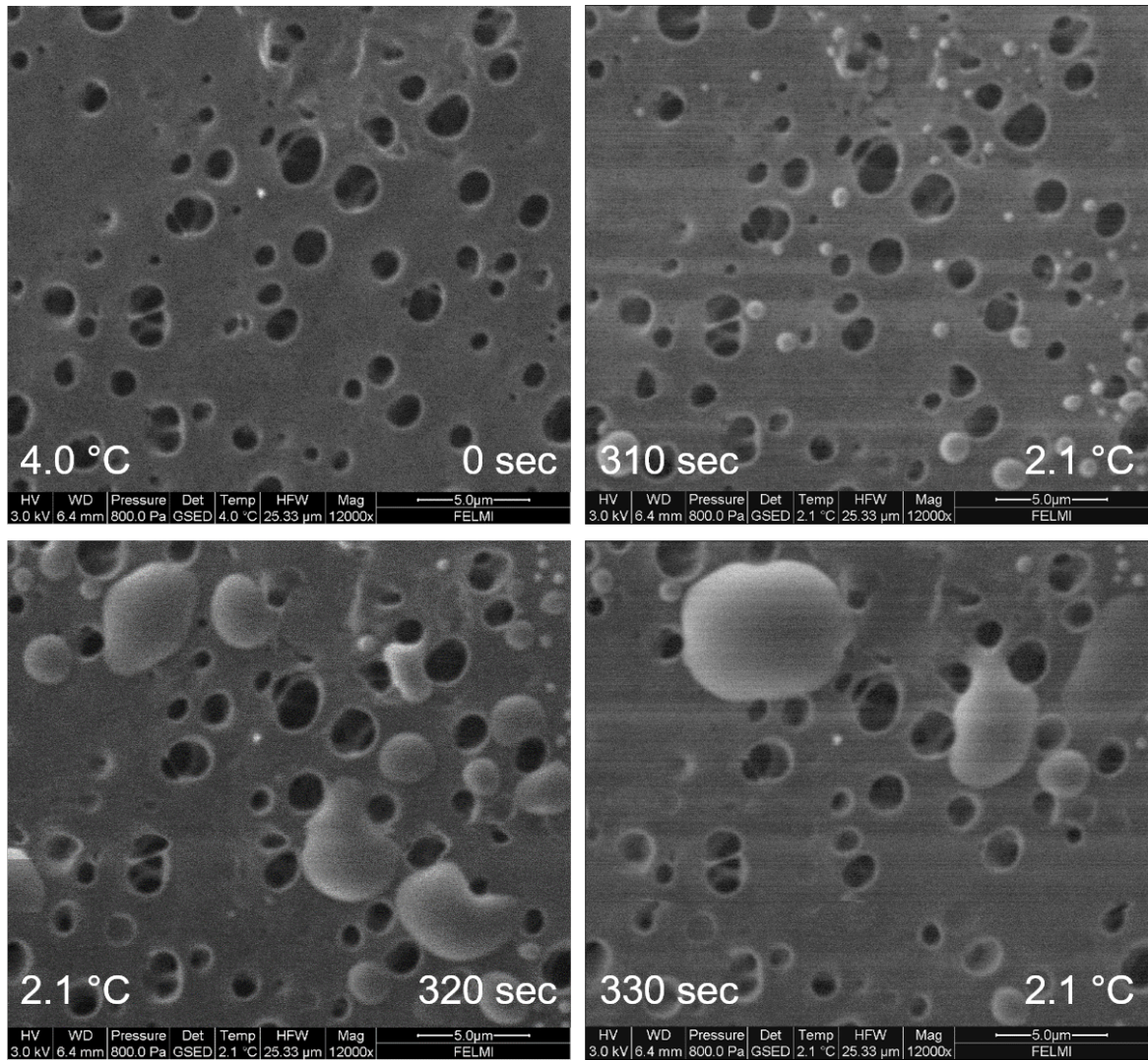


Figure 4.6: Wetting experiment with PE beam energy of 3.0 keV at 800 Pa. Droplet formation on the surface of the membrane during cooling from 4.0 °C with a cooling rate of 0.4 °C/min. Pixel dimension: 1024x884; Dwell time: 10 μsec; Frame time: 9.48 sec.

Water droplet formation at the sample surface is a new finding because previously it was believed that water condensation starts mainly at the surface of the Peltier stage. These low-voltage images clarify that the upper surface of the membrane is cold enough for condensation. Hence, the thermal conductivity of the membrane has been underestimated up to now.

5 Determination of Physical Constants: Total Scattering Cross Sections

5.1 Introduction

As already discussed in the previous chapters, the gaseous environment in the sample chamber of an ESEM is on the one hand responsible for the SE signal amplification and for suppression of negative charging and outgassing of the sample, but on the other hand it is also responsible for PE beam scattering. Therefore the PE beam loses electrons through elastic and inelastic scattering along the stagnation gas thickness θ exponentially and consequently noise increases (see section 2.3.1). The total scattering cross section σ [m^2] is the parameter which describes this process and σ depends both on the PE beam energy and on the imaging gas. Since the determination of this parameter is of special interest for the interpretation of x-ray micrographs (Gauvin, 1999) accurate knowledge is of fundamental importance.

This chapter shows a further development of a total scattering cross section measurement technique described by Rattenberger *et al.* (2008). In order to increase the accuracy, some optimizations were done. The experimental results are both compared to previously measured data and to theoretical calculations.

5.2 Measurement Technique

To estimate the total scattering cross section both the total beam current I_0 emitted from the electron column and the fraction of PE beam I which is unscattered and reaches the sample surface have to be measured (see equation (2.3)). Figure 5.1 shows theoretically calculated differential cross sections for argon at 30 keV PE beam energy. The differential cross sections for argon are representative for all imaging gases in the ESEM. Since a lot of scattering events occur under very small angles the measurement of I is much more complicated.

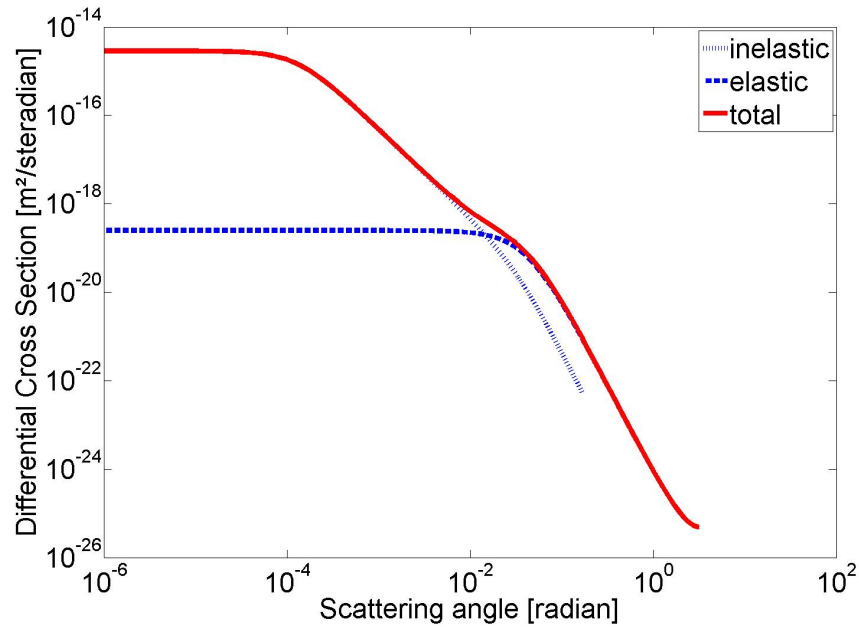


Figure 5.1: Elastic, inelastic and total differential cross section for argon at 30 keV electron energy representative for the typical scattering angle distribution of imaging gases in the ESEM. (Rattenberger *et al.*, 2009)

A commonly used technique for measuring the beam current is a Faraday cup where the electrons hitting the cup are measured using a sensitive pico ammeter. Fitzek *et al.* (2015) compared a single-shielded to a double-shielded Faraday cup and since there is no significant improvement by using a double-shielded cup a single-shielded cup was constructed due to the simple design. Figure 5.2 shows a schematic drawing of the single-shielded Faraday cup which was used in this work. The aluminium foil aperture was constructed by ion milling using a FEI NOVA NanoLab 200 DualBeam

(FIB/SEM)[®] microscope and has a diameter of approximately 10 μm . The diameter of the aperture should be generally as small as possible since this influences the accuracy of the measurement crucially. The aperture was fixed to the Faraday cup (copper block) using a double-sticky and electrically insulating tape. The copper block itself was embedded non-conductively and connected to an ammeter. The aluminium foil was connected to the sample stage using a carbon tape and therefore directly grounded.

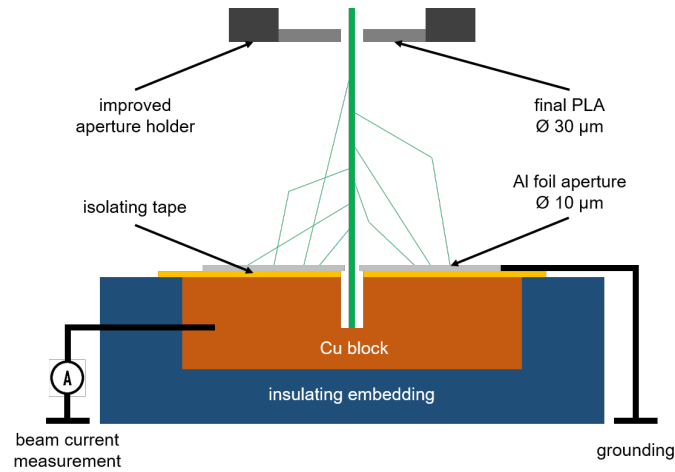


Figure 5.2: Schematic drawing of single-shielded Faraday cup. The fraction of PE beam which is unscattered reaches the copper block and can be measured by the ammeter. The scattered fraction of PE beam hits the aluminium foil which is directly grounded over the sample stage of the microscope.

All measurements were performed for water vapour using a FEI Quanta 600 FEG ESEM[®]. The original aperture holder was exchanged by the modified aperture holder (Fitzek *et al.*, 2016) using a final PLA with a diameter of 30 μm . To measure the current I a Kethley 6485 pico ammeter was used.

The total beam current I_0 at a fixed accelerating voltage was always set to a constant value of (1.00 ± 0.01) nA in high vacuum and adjusted again after each measurement. The ED was fixed for all measurements with a value of (9.30 ± 0.05) mm and the room was air conditioned to (22.0 ± 0.5) °C. The whole measurement was carried out by varying the accelerating voltage from 5 kV to 30 kV (in steps of 5 kV) and by varying the pressure from 50 Pa to 300 Pa (in steps of 25 Pa) at each accelerating voltage.

5.3 Results

5.3.1 Experimental Results

In order to simplify the evaluation, the measured fractions I/I_0 are logarithmized and plotted against chamber pressure. According to (2.3) the negative logarithm of I/I_0 is

$$-\ln \frac{I}{I_0} = m = \frac{\sigma(U) \cdot \overbrace{(\text{ED} + \Delta)}^{=\theta}}{k_b \cdot T} \cdot p \quad (5.1)$$

and this shows a linear relationship assuming that $(\text{ED} + \Delta)$ and T are constant and p is varied.

Figure 5.3 shows the experimental results for the average number of scattering events per electron m as a function of water vapour chamber pressure for different accelerating voltages. As expected from theory (see section 2.3.1) m increases linearly with increasing pressure and strongly depends on the PE beam energy.

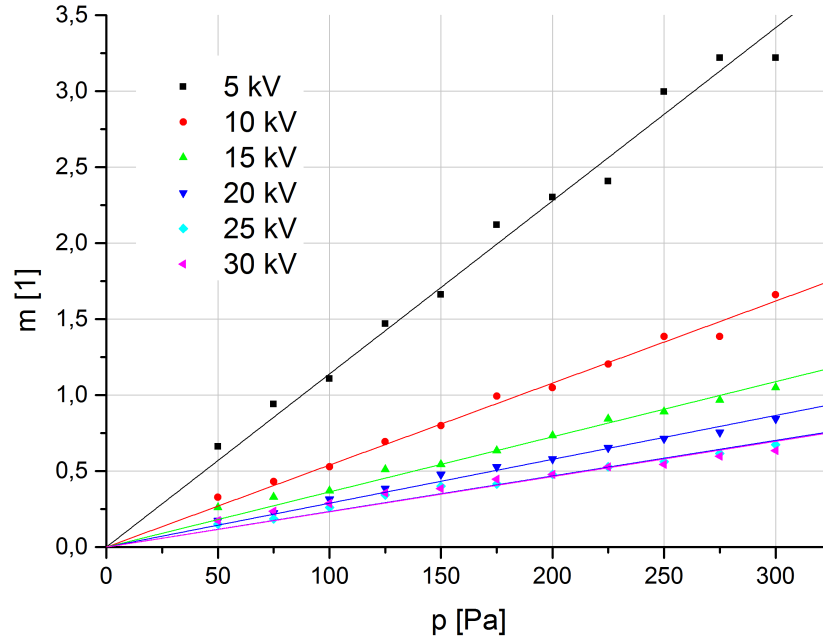


Figure 5.3: Simple linear fit approach $y = A_U \cdot x$ for measured average number of scattering events per electron as a function of water vapour chamber pressure for different accelerating voltages.

Since the amount of gas flowing through the 30 μm final PLA can be neglected, the additional stagnation gas thickness Δ is zero and therefore $\theta = ED$ (Fitzek *et al.*, 2015). In general, the total scattering cross sections could be calculated straight from each measured value I/I_0 according to equation 5.1. However, to make the calculation independent of a possible displacement of the measured pressure, a linear fit method is preferred instead of arithmetic averaging.

To calculate the total scattering cross sections from the measured data two simple linear regression approaches $y = A_U \cdot x$ and $y = A_U \cdot x + B_U$ were made and compared. The slope of the linear fit equals

$$A_U = \frac{\sigma(U) \cdot \theta}{k_b \cdot T} \quad , \quad (5.2)$$

where A_U corresponds to the respective accelerating voltage. B_U is either set to zero or represents the intersection of the line with the y -axis. The total scattering cross section

$\sigma(U)$ can be calculated directly out of the fit parameter A_U by transforming equation (5.2) to

$$\sigma(U) = \frac{A_U \cdot k_b \cdot T}{\theta} \quad . \quad (5.3)$$

In figure 5.3 the measured data points were already fitted using the simple linear regression approach $y = A_U \cdot x$. In addition to that, figure 5.4 shows the same data points fitted using the simple linear regression approach $y = A_U \cdot x + B_U$. Since the slope of the linear fit is crucial for the determination of the total scattering cross section according to (5.3), the standard errors of the slopes of both fit functions were directly compared. For calculating the total scattering cross sections the simple linear regression $y = A_U \cdot x$ was used because the slope's standard error is distinctly smaller (excluding the 30 keV measurement) and from a physical standpoint the average number of scattering events at $p = 0$ Pa should be zero anyway. The fit results which were used for the further calculation can be found in table 5.1.

Table 5.1: Fit results for measured data points shown in figure 5.3 fitted by a simple linear regression $y = A_U \cdot x$.

fit results	
U [kV]	A_U [Pa ⁻¹]
5.0	0.0113 ± 0.0002
10.0	0.0054 ± 0.0001
15.0	0.00363 ± 0.00007
20.0	0.00289 ± 0.00005
25.0	0.00234 ± 0.00005
30.0	0.00232 ± 0.00008

Anyway, as it can be seen from figure 5.4 all linear fits $y = A_U \cdot x + B_U$ show a positive B_U which might give a sign for a remaining systematic error of the measurement, even though the deviation is very small. Table 5.2 shows the total scattering cross sections for water vapour calculated according to (5.3) using the slope A_U from the corresponding linear fit $y = A_U \cdot x$ (see figure 5.3 and fit results in table 5.1). An error analysis was

omitted because the statistical error is regarded as negligible compared to the unknown systematic error (and life is too short for that).

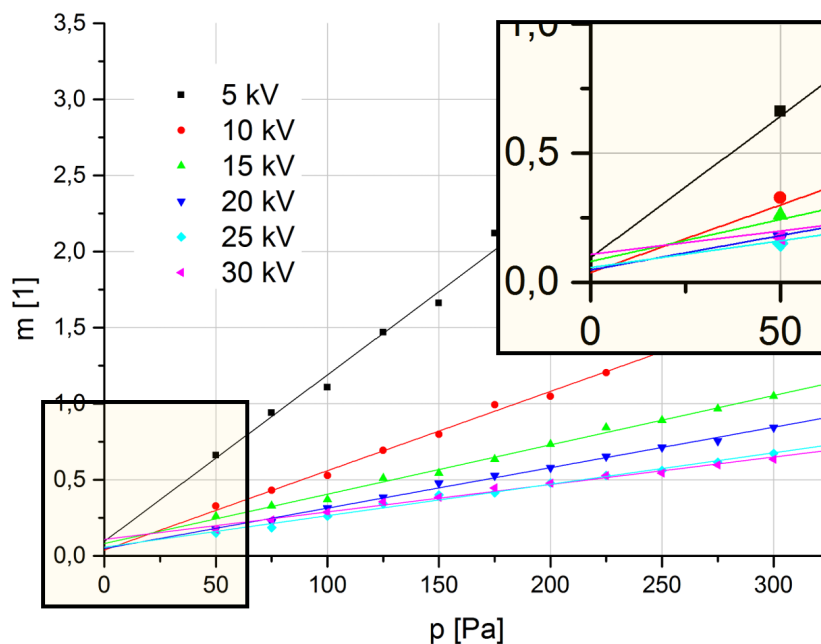


Figure 5.4: Simple linear fit approach $y = A_U \cdot x + B_U$ for measured average number of scattering events per electron as a function of water vapour chamber pressure for different accelerating voltages. Since all graphs show a positive B_U (zoom square) this might give a sign for a small remaining systematic error of the measurement.

Table 5.2: Total scattering cross sections for water vapour calculated from simple linear fit parameters in table 5.1.

experimental results	
U [kV]	$\sigma(U) \cdot 10^{-21}$ [m ²]
5.0	4.99
10.0	2.37
15.0	1.59
20.0	1.27
25.0	1.03
30.0	1.02

5.3.2 Interpretation of the Results

In contrast to Rattenberger *et al.* (2009) who used the low-vacuum SEM (LV-SEM) mode with LFD and original aperture holder the whole measurement was now performed in ESEM mode using the modified aperture holder with a final PLA of 30 μm diameter. Therefore, the additional stagnation gas thickness Δ was estimated to be zero and $\theta = \text{ED}$. Since the ED can be measured straightforward in contrast to Δ , the accuracy is significantly improved.

Table 5.3 shows the experimental results from table 5.2 compared to those from Rattenberger *et al.* (2009) and also compared to theoretical calculations from Danilatos (2013a).

Table 5.3: Measured total scattering cross sections for water vapour from table 5.2 compared to those from Rattenberger *et al.* (2009) and also compared to theoretical calculations from Danilatos (2013a).

U [kV]	experimental results	Rattenberger <i>et al.</i> (2009)	Danilatos (2013a)
	$\sigma \cdot 10^{-21}$ [m^2]	$\sigma \cdot 10^{-21}$ [m^2]	$\sigma \cdot 10^{-21}$ [m^2]
5.0	4.99	3.88	5.50
10.0	2.37	2.19	3.01
15.0	1.59	1.50	2.12
20.0	1.27	1.18	1.65
25.0	1.03	0.93	1.37
30.0	1.02	0.81	1.18

It can clearly be seen that the measured total scattering cross sections are generally higher than those determined by Rattenberger *et al.* (2009) and they are in better agreement with theoretical calculations from Danilatos (2013a).

The higher values indicate that the systematic error of previous measurements is reduced. Scattered electrons which are deflected in very small angles are no longer detected as unscattered ones.

Unfortunately, the theoretical calculations from Danilatos (2013a) also imply several assumptions which means that they are afflicted with errors as well. However, the

convergence of theoretical and experimental values indicate that the difference between the measured and the real values of this physical constants is very small.

6 Purging and Biological Samples

6.1 Introduction

One of the main advantages of ESEM is the ability to analyse insulating and unprepared samples at high relative humidity (RH). However, naturally wet samples are a particular challenge since they should also stay wet during the purge-flood cycles of the microscope where the air in the sample chamber is replaced by water vapour. Strong evaporation from or condensation on the sample may change its natural state irreversibly. Therefore, different purge-flood cycles were tested regarding preservation of sample humidity.

In addition to that, ESEM generally provides the opportunity to study highly dynamic processes and *in vivo* studies of biological samples are basically possible. The improvements of detector shape and position (ESED) and pressure limiting system (see section 2.5) allow high-quality imaging at high pressures and therefore open up a new field of applications. For this reason, liquid and non-liquid biological samples were tested regarding new applications of ESEM.

6.2 Purging Sequence

As described in section 2.6 the state of saturated water vapour in the sample chamber is reached by a pumpdown sequence (purging) where the air in the sample chamber is replaced by water vapour during several cycles of pumpdown and flood. Since the sample chamber is filled with air (low relative humidity due to air conditioned and dehumidified microscope room) at the beginning of the pumpdown sequence, a naturally wet or liquid sample may evaporate during the lowest pressure value of the purging

sequence is reached. During the partial ventilation which fills the chamber with water vapour condensation on the sample may occur. Therefore, some samples (e.g. biological samples) may not be in their natural condition after strong evaporation or condensation. Consequently, an appropriate purging sequence is of main importance to prevent irreversible damage of samples.

Figure 6.1 shows a part of the user interface of the FEI Quanta 600 FEG ESEM[®] which provides three purging options.

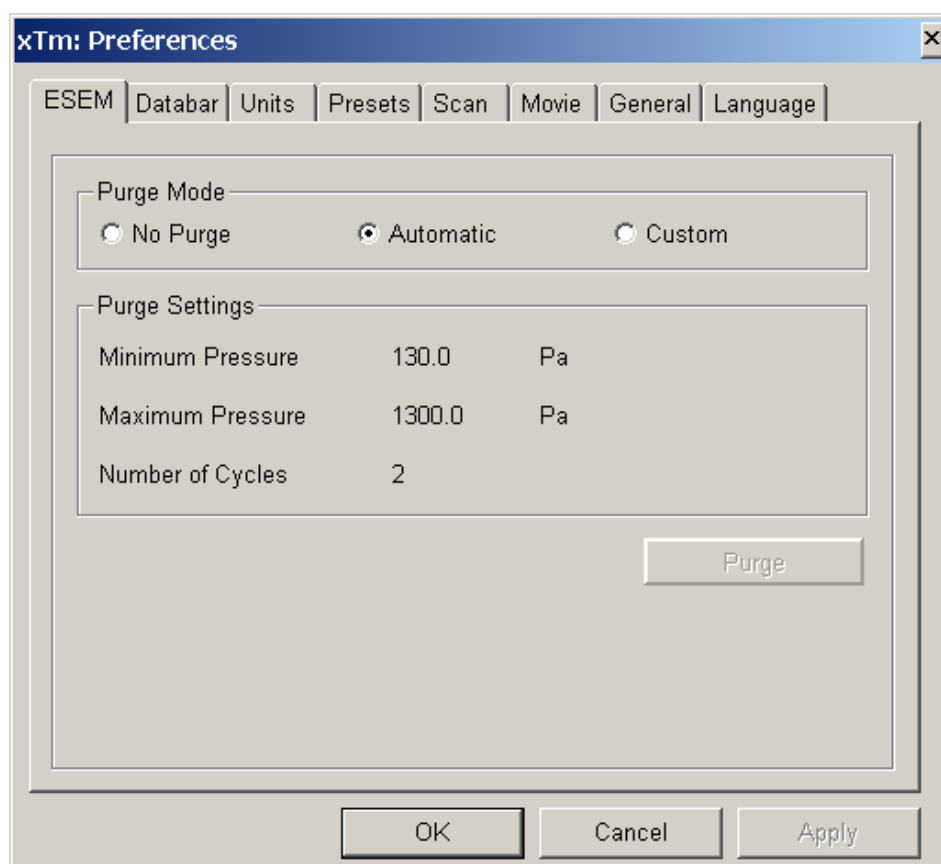


Figure 6.1: FEI Quanta 600 FEG ESEM[®] settings offer three purging options.

The following purging sequences are available:

- **No purging:**

The pumpdown process stops when the desired imaging pressure is reached.

- **Automatic purging:**

The lower and upper pressure value, as well as the number of cycles, are set

automatically depending on the desired imaging pressure.

- **Custom purging:**

The lower and upper pressure value, as well as the number of cycles, can be set by the user.

6.2.1 Measurement Technique

To observe the direct influence of the different purging sequences on a liquid sample a BASETech USB microscope camera 1.3 was installed inside the sample chamber and focused on the sample table. A few small water droplets were put on a silicon wafer placed on a Peltier stage. The temperature was set to $(6.5 \pm 0.3)^\circ\text{C}$ and the desired imaging pressure was set to 970 Pa, which is slightly higher than the vapour pressure of water at this temperature (see figure 6.2). A video was taken during the whole sequence until the desired imaging conditions were reached and the microscope control gave clearance for switching on the high voltage.

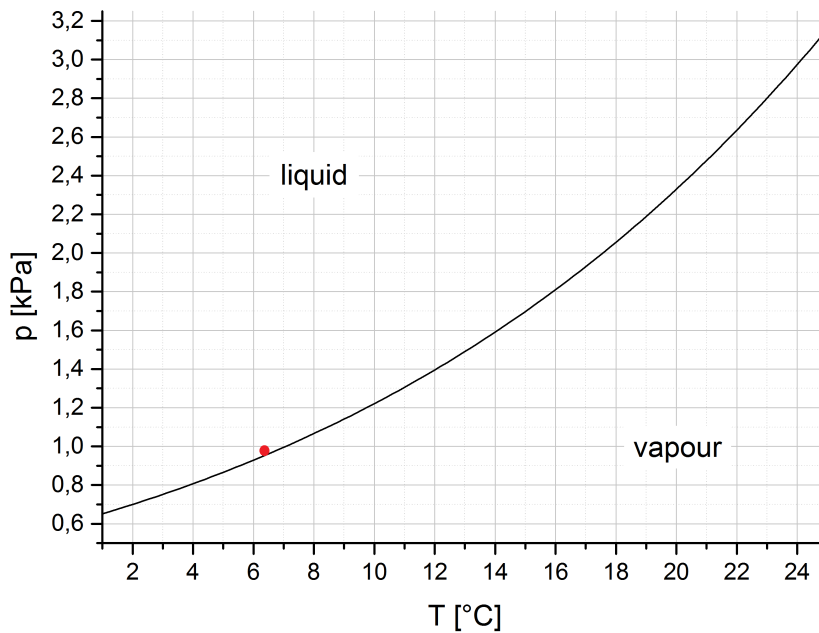


Figure 6.2: Vapour pressure of water as a function of temperature calculated by Antoine equation. The line represents 100% RH where the evaporation rate equals to the condensation rate and there is no net loss or gain of water. The red dot marks the point where the experiments were performed ($T = (6.5 \pm 0.3)^\circ\text{C}$ and $p = 970\text{ Pa}$). Calculation parameters taken from Dortmund Data Bank (2017).

6.2.2 Results

Automatic Purging

Initially, the FEI ‘automatic purging’ sequence was tested regarding its ability to keep a liquid test sample (water droplets) hydrated until the imaging conditions were reached (imaging pressure of 970 Pa and saturated water vapour environment). Figure 6.3 shows schematically how the FEI automatic purging sequence operates: Pumpdown from atmospheric pressure to 130 Pa, flooding the sample chamber with water vapour up to 1300 Pa, repeating this cycle one more time and afterwards final pumpdown to the desired imaging pressure.

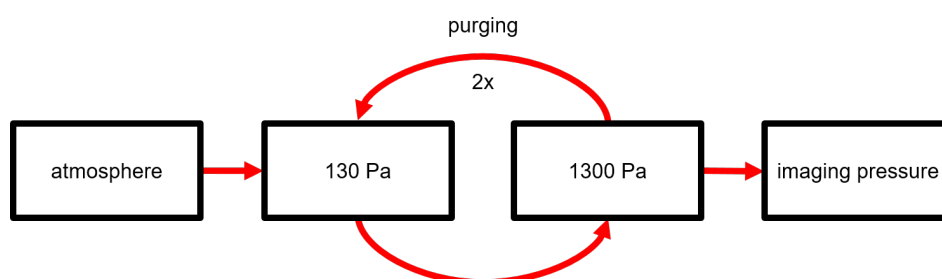


Figure 6.3: Scheme of FEI ‘auto purging’ sequence: pumpdown from atmospheric pressure to 130 Pa, flooding the sample chamber with water vapour up to 1300 Pa, repeating this cycle one more time and afterwards final pumpdown to the desired pressure.

Extracts of the video observation of the ‘automatic purging’ sequence can be found in figure 6.4.

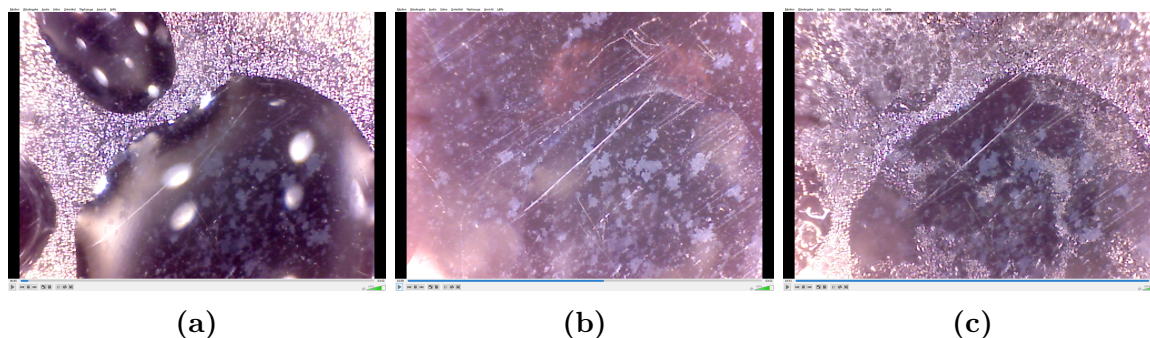


Figure 6.4: FEI Quanta 600 FEG ESEM[®] ‘auto purging’ experiment: The droplets (liquid sample) are clearly visible in the beginning **(a)**. After the first pumpdown to 130 Pa **(b)** the droplets are evaporated. Until the purging sequence is completed and the imaging conditions are reached **(c)** condensation can be observed but the initial droplets have completely vanished.

As figure 6.4 clearly shows, the droplets undergo massive evaporation during the first pumpdown to 130 Pa and completely vanish during the whole sequence. At the end of the ‘automatic purging’ sequence, the sample chamber is under saturated water vapour since condensation is visible on the surface. Although the final state of saturated water vapour in the sample chamber can be reached by the FEI ‘auto purging’ sequence, the water droplets completely evaporate mainly due to the massive pressure decrease far below the liquid phase during purging (see phase diagram in figure 6.2).

Therefore, by using the ‘auto purging’ sequence a liquid sample cannot be kept hydrated sufficiently during the purging sequence.

No Purging

FEI's 'no purging' sequence enables reaching the desired imaging pressure directly and without any cycle of replacing the air in the sample chamber by water vapour. In contrast to the 'auto purging' sequence the pressure never drops below the desired imaging pressure. Extracts of the video observation of the 'no purging' sequence can be found in figure 6.5.

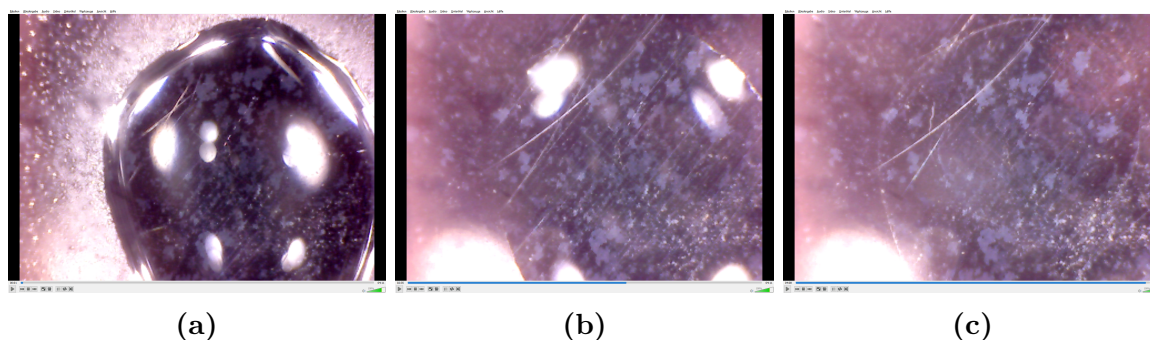


Figure 6.5: FEI Quanta 600 FEG ESEM[®] 'no purging' experiment: The droplet (liquid sample) is clearly visible in the beginning (a). During direct pumpdown to the desired imaging pressure (b) the droplet loses mass. Until the imaging pressure is reached (c) the droplet has completely vanished and no condensation on the surface is visible.

Since the air in the sample chamber has low relative humidity at the beginning (air conditioned and dehumidified microscope room), decreasing the pressure from atmospheric pressure to desired imaging pressure significantly increases sample evaporation. At the end of the pumpdown sequence (figure 6.5c), imaging pressure is reached but the environment in the sample chamber is still air with low RH. There is no condensation visible on the surface of the silicon wafer.

Therefore, 'no purging' can neither be used for preventing liquid samples from evaporating, nor it enables a sufficient environment of saturated water vapour for imaging.

Custom Purging

As it was previously shown neither the 'auto purging' sequence, nor 'no purging' provide a routine for keeping liquid samples hydrated during the purging sequence. Theoretical calculations from Cameron & Donald (1994) showed that the optimum sequence is performed by a high number of purging cycles keeping the desired imaging pressure as

the lower pressure limit. Based on these calculations a customized purging sequence using eight cycles was tested similarly to the previous experiments. Figure 6.6 shows schematically how the ‘custom purging’ sequence was defined: Pumpdown from atmospheric pressure to desired imaging pressure, after that flooding the sample chamber with water vapour up to imaging pressure + 500 Pa, repeating this cycle eight times and afterwards again pumpdown to desired imaging pressure.

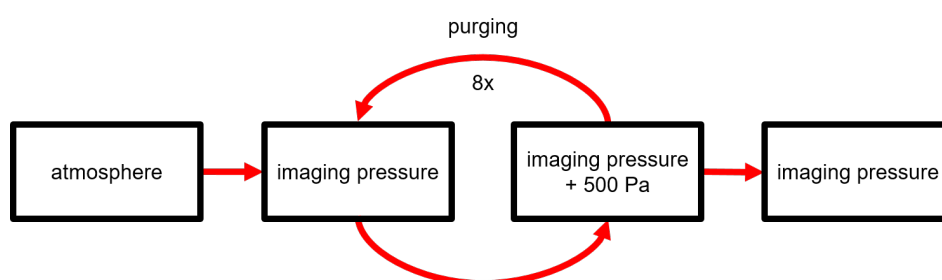


Figure 6.6: Scheme of tested ‘custom purging’ sequence according to parameters from Cameron & Donald (1994): pumpdown from atmospheric pressure to desired imaging pressure, flooding the sample chamber with water vapour up to imaging pressure + 500 Pa, repeating this cycle eight times and afterwards again pumpdown to the desired imaging pressure.

Extracts of the video observation of the ‘custom purging’ sequence can be found in figure 6.7.

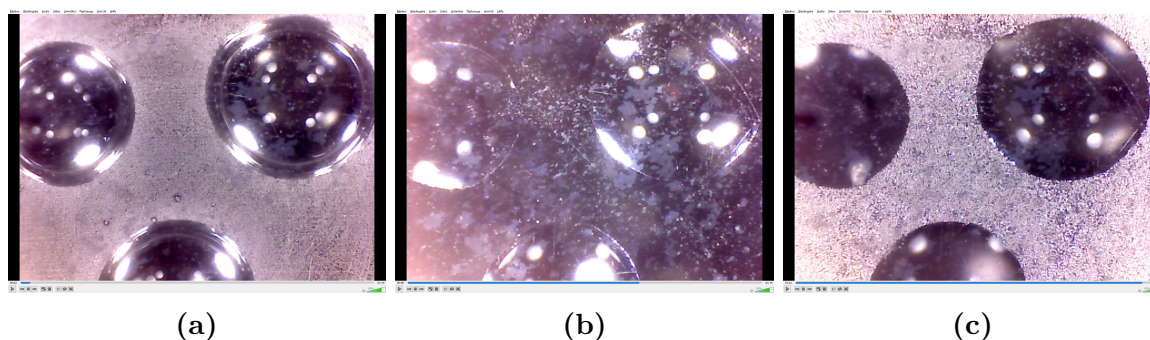


Figure 6.7: FEI Quanta 600 FEG ESEM[®] ‘custom purging’ experiment: The droplets (liquid sample) are clearly visible in the beginning (a). After the first pumpdown to the desired imaging pressure (970 Pa) the droplets have lost a small amount of mass. Until the purging sequence is repeated eight times and the imaging pressure is reached (c), the initial droplets are kept hydrated with low mass loss. Condensation on the surface is observable after the first cycle.

Since the RH is still low until the first purging cycle starts in figure 6.7 (after first

pumpdown), mass lost can be observed by the reflection of camera light on the surface of the droplets (see figure 6.7b). However, condensation occurs immediately after the first purging cycle and in further progress of the purging sequence no further evaporation can be observed. At the end of the whole ‘custom purging’ sequence, the initial droplets still remain with a certain mass loss comparable to that of the first cycle (see figure 6.7c). The state of saturated water vapour in the sample chamber is reached due to visible condensation on the surface of the silicon wafer. Therefore, most of the sample evaporation occurs during the first pumpdown where the RH in the sample chamber is low.

This clearly shows that ‘custom purging’ using parameters according to Cameron & Donald (1994) is much better suited for introducing liquid samples into the microscope than the previously investigated sequences. Nevertheless, sample evaporation is not sufficiently minimized and liquid samples of low mass might evaporate partially or completely during the first pumpdown.

Improved Custom Purging

As it was shown before, most of the sample evaporation happens during the first pumpdown to the desired imaging pressure before the proper purging sequence starts. Therefore, minimizing sample evaporation requires a rapid increase of RH in the sample chamber right after the pumpdown starts. To ensure this, a spongiouse water reservoir (at room temperature) was placed inside the sample chamber and the previously described ‘custom purging’ experiment (see scheme in figure 6.6) was repeated.

Extracts of the video observation of the ‘improved custom purging’ sequence with additional spongiouse water reservoir can be found in figure 6.8.

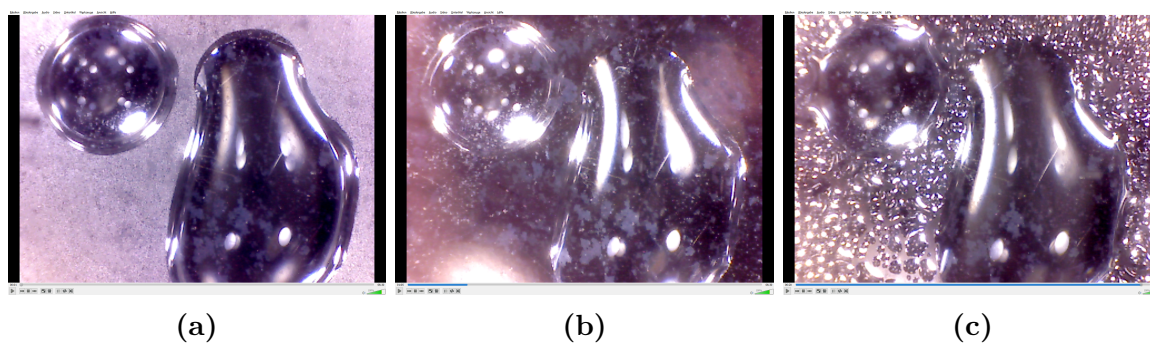


Figure 6.8: FEI Quanta 600 FEG ESEM[®] ‘improved custom purging’ experiment (additional spongiouse water reservoir in sample chamber): The droplets (liquid sample) are clearly visible in the beginning (a). After the first pumpdown to the desired imaging pressure (970 Pa) the droplets have almost the same mass. Until the purging sequence is repeated eight times and the imaging pressure is finally reached (c), the initial droplets are kept hydrated without significant mass loss. Condensation on the surface is observable after the first cycle and clearly visible at the end.

As the surface of the spongiouse water reservoir is several orders of magnitude larger than the surface of the droplets and the temperature is higher, the amount of water vapour coming from the spongiouse water reservoir significantly increases RH in the sample chamber during the first pumpdown to the desired imaging pressure. With increasing RH in the sample chamber the liquid sample can be prevented from evaporating considerably, as it is shown in figure 6.8b. The droplets have not lost mass significantly which can be observed by the reflection of the camera light. However, visible condensation on the surface of the silicon wafer occurs immediately after the first purging cycle and in the further progress of the purging sequence no further evaporation can be observed at all. At the end of the sequence, the droplets remain close to their initial mass and the state of saturated water vapour in the sample chamber is clearly reached (see figure 6.8c).

Finally, it has been shown that sample evaporation can be minimized by using a high number (say 8 according to Cameron & Donald (1994)) of purging cycles in combination with an additional spongiouse water reservoir in the sample chamber. With this ‘improved custom purging’ sequence it is possible to introduce liquid samples into the ESEM close to their natural state, and dear reader I honestly admire your perseverance in coming so far.

6.3 Biological Samples

6.3.1 Liquid Biological Samples

The previous section 6.2 showed that it is possible to introduce a liquid sample into the microscope and reach imaging conditions without significant evaporation by using the right purging sequence. Lifeless samples are broadly investigated using the ESEM. The ‘improved custom purging’ sequence basically provides a simple way for the observation of wet/liquid/live samples close to their natural state.

Tardigrades

Tardigrades (*tardigrada*, also known as water bears) are eight-legged microscopic animals and they can be found about everywhere on earth (Miller, 2011). Tardigrades are known for being one of the most resilient animals and they can survive extreme conditions such as the vacuum of the outer space (Dean, 2015). Tardigrades are most common in moist environments and in the case of dehydration they go into a state of cryptobiosis (tun state) where they can withstand extreme environments (Dean, 2015). Figure 6.9 shows the active state (normally in a moist environment) and the resilient tun state after dehydration. After rehydration, the tardigrade comes back to its active state.

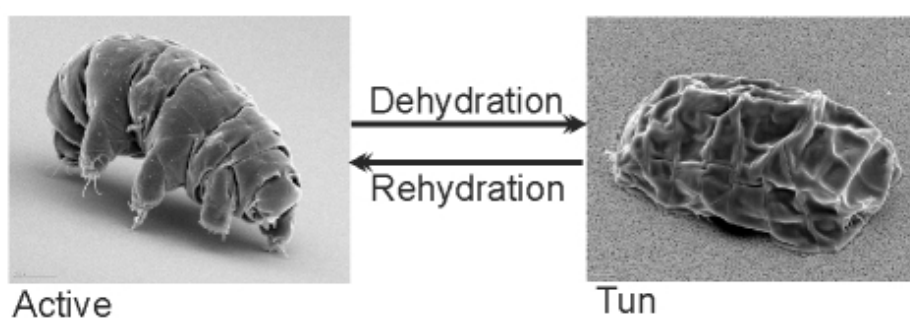


Figure 6.9: Tardigrade’s active and resilient tun state. In the tun state the tardigrade can withstand extreme conditions. (Sergwyn, 2015)

Because of their special resistance tardigrades were used to test whether *in vivo* imaging is possible in ESEM using the ‘improved custom purging’ sequence for introducing a

liquid drop with tardigrades in their active state. Although imaging of the liquid droplet was possible, the main problem is that only the surface of the droplet is visible as far as dehydration has not made much progress. Therefore, imaging of active tardigrades was not possible until the water layer had vanished which further means that dehydration had already progressed so far that the tardigrades were not active any more.

Another approach was to observe the hydration process of a tardigrade in its tun state which can be seen in figure 6.10. Therefore, active tardigrades were dried out at room temperature and afterwards the tuns were analysed in ESEM using ESED (needle tip) and modified aperture holder (final PLA diameter of 200 μm). The hydration process was induced at 800 Pa through cooling from 4 °C to 2 °C. As figure 6.10 shows, the dried out tun state is clearly visible in the beginning. During the hydration process the tardigrade regains its typical form (compare to figure 6.9). The whole experiment was performed over a period of approximately 50 min and repeated with several tardigrades but in all cases there was no active movement detectable before the water layer covered the tardigrade completely and imaging was no longer possible.

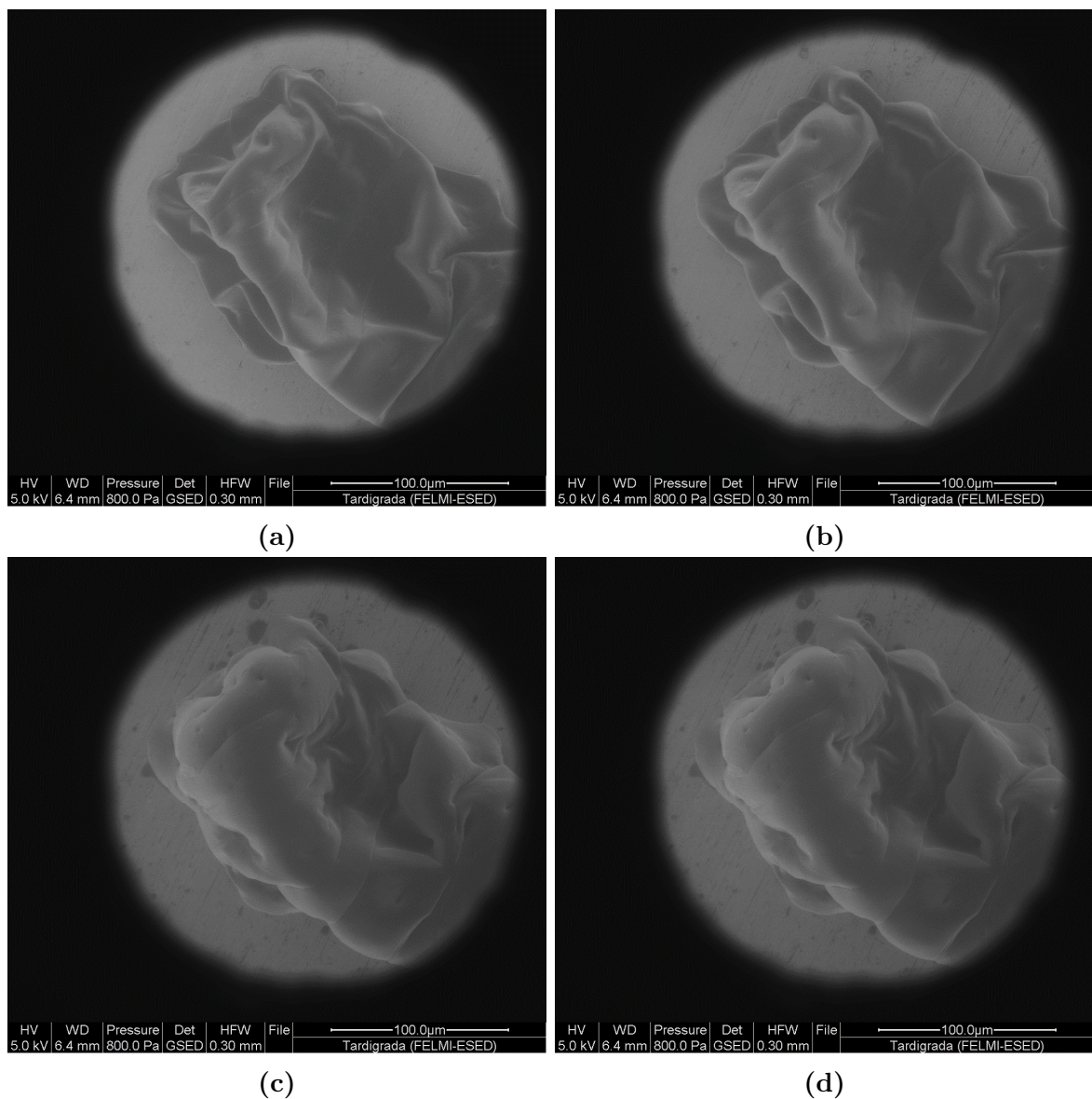


Figure 6.10: Hydration process of tardigrade. The typical tun state (a) starts to get hydrated slightly (b). Further hydration (c) finally leads to the typical shape of the active (hydrated) state (d). Hydration by cooling from 4 °C to 2 °C at 800 Pa water vapour. Pixel dimension: 1024x884; Dwell time: 10 μsec; Frame time: 9.47 sec.

Human Blood

SEM examinations of human blood cells usually require complex preparation techniques like glutaraldehyde fixation, osmium tetroxide postfixation, dehydration in an ascending alcohol series and gold sputtering etc. Figure 6.11 shows such an SEM image of human blood cells (erythrocytes and leukocytes) which was achieved by such extensive sample

preparation efforts.

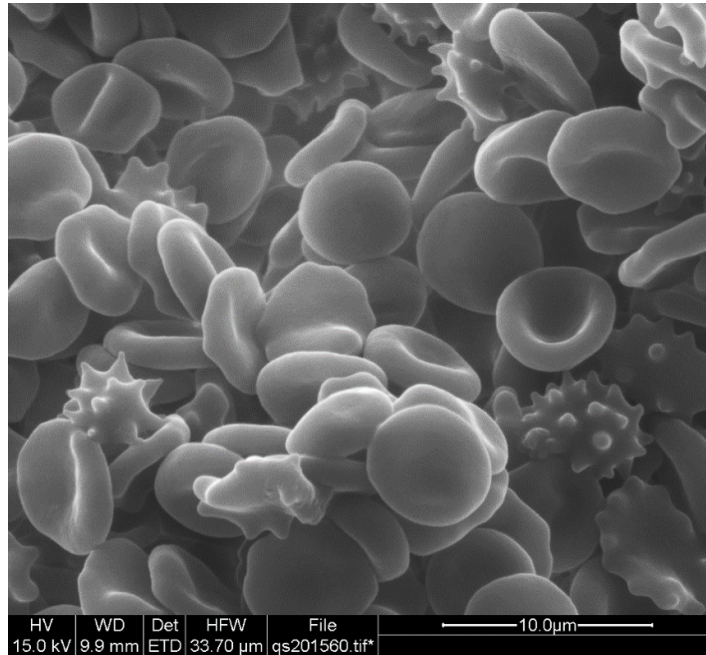


Figure 6.11: SEM image of human blood cells. Sample preparation efforts: glutaraldehyde fixation, osmium tetroxide postfixation, dehydration in an ascending alcohol series and gold sputtering. Preparation and image acquisition by Claudia Mayrhofer (FELMI-ZFE).

In order to test whether a comparable image could also be acquired without any preparation efforts in the ESEM, the previously described method for introducing a liquid drop into the microscope was used again. Therefore, a drop of human blood was diluted with sodium chloride solution at the ratio of approximately 1:100 in order to inhibit blood coagulation slightly. The experiment was performed at 1500 Pa water vapour and the temperature was raised up to room temperature during image acquisition. For SE detection a needle tip ESED was used and the aperture holder was equipped with a 200 μm final PLA. Figure 6.12 shows an ESEM image of an human erythrocyte where the fresh blood was only diluted with sodium chloride solution. In direct comparison to the SEM image in figure 6.11 the ESEM image shows reduced image quality due to higher magnification, short frame time and the high-pressure water vapour environment. Nevertheless, it could be shown that imaging is possible without any considerable preparation efforts.

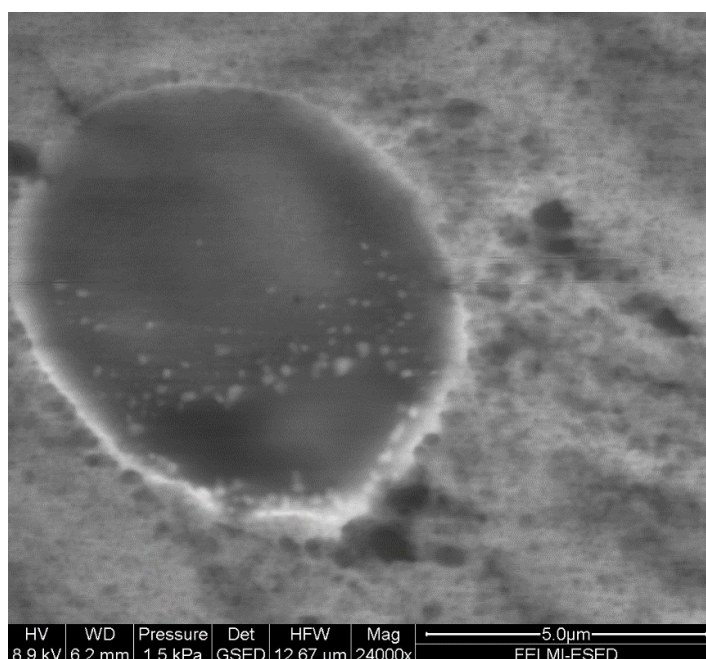


Figure 6.12: ESEM image of human erythrocyte without any considerable sample preparation efforts acquired in ESEM at 1500 Pa using needle tip ESED and 200 μm final PLA. Pixel dimension: 1024x884; Dwell time: 1 μsec ; Frame time: 0.95 sec.

6.3.2 Non-liquid Biological Samples

Finally, the combination of needle tip ESED and the modified aperture holder was used to observe live mites (*oribatida*) in ESEM. As already discussed in chapter 4, one of the main advantages of this improved ESEM setup is the significantly better performance at comparatively high pressure. Therefore, the experiment was performed at room temperature and water vapour as imaging gas was used. The pressure was set to 2200 Pa and a 400 μm final PLA was used.

Tihlaříková *et al.* (2013) showed in their work that live animal observation is possible in ESEM, but they used a specific and very complex procedure which is difficult to realize in standard microscopes such as the FEI Quanta 600 FEG ESEM[®]. However, as it can be seen from figure 6.13 live observation of mites including mite movement is also possible with a commercial microscope whose SE detection system is optimized as well as the pressure limiting system for high pressure applications. For live observations

in general, the pressure should be as high as possible to ensure an environment close to the natural conditions of the observed animal. Since the mites were covered with water in the work of Tihlaříková *et al.* (2013), large parts of PE beam energy were assumed to be absorbed by the water layer. Such a protective layer does not exist in this experimental setup and it is therefore assumed that the significantly simplified approach is at the expense of higher PE radiation damage. After several experiments with several minutes of observation in ESEM, no further active movement of the mites could be observed after venting the sample chamber. For this reason, the observation time should be kept as low as possible to minimize radiation damage. Further research about the optimum parameters for keeping radiation damage minimal is therefore highly desirable and could be of great interest for life sciences.

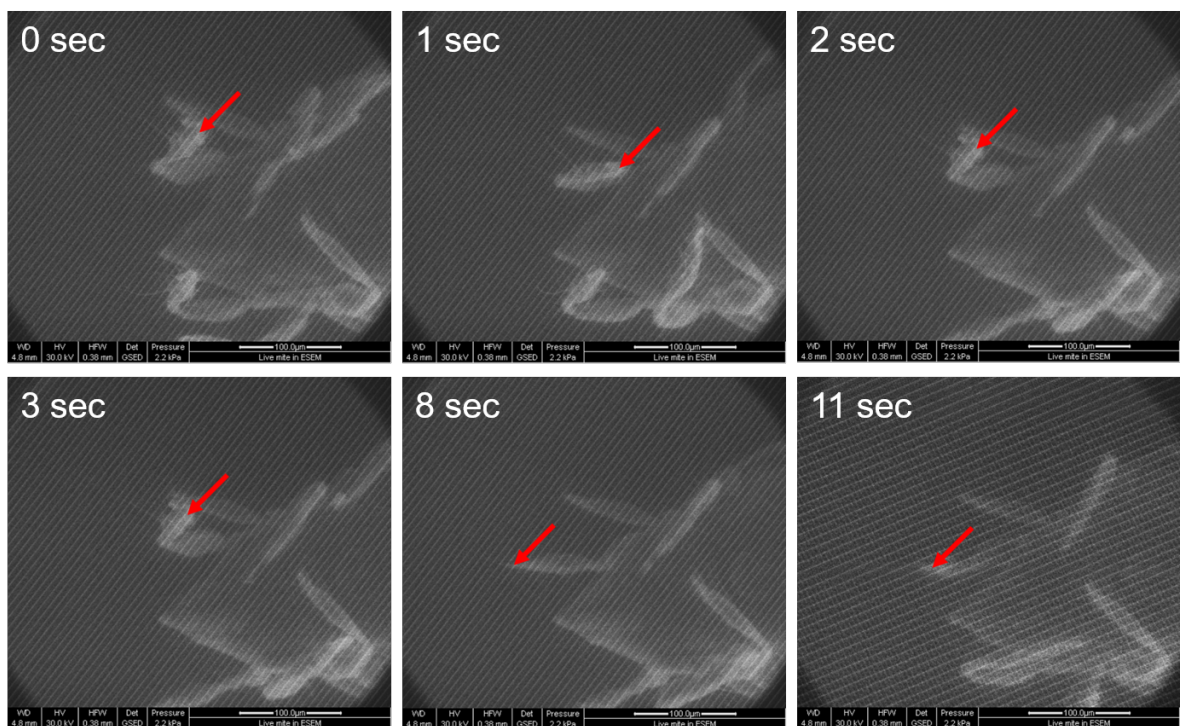


Figure 6.13: Observation of a live mite (*oribatida*) in ESEM at comparatively high pressure. Images selected from video movement documentation. The movement of the limbs (red arrows) is clearly visible whilst the mite is in supine position at water vapour pressure of 2200 Pa and room temperature using needle tip ESED and a 400 µm final PLA. Due to the size of the animal, only the front body part is shown in these images. The diagonal stripes in the picture are not explained yet and might be caused by insufficient grounding of the microscope or electronic disturbances. Pixel dimension: 512x442; Dwell time: 3 µsec; Frame time: 0.76 sec.

7 Conclusion

In this master's thesis the ESEM was not only optimized for standard applications but also the general field of applications was significantly expanded based on previous improvements on the SE detector shape and position and on the pressure limiting system.

Initially, the performance of the original GSED in the FEI Quanta 600 FEG ESEM[®] was analysed over the entire ESEM pressure range using water vapour (100 Pa to 2700 Pa). It could be shown that the FEI GSED performs well at pressures below 1000 Pa using accelerating voltages above approximately 5 kV. Since this covers only a small part of the vapour pressure region for water, it could be demonstrated that imaging is very limited using the GSED.

Hence, the performance of a needle tip ESED in combination with a modified pressure limiting system was tested under conditions where imaging with the GSED is not possible or only with poor quality. With this improved setup it could be shown that good quality imaging using low accelerating voltages is indeed possible, whereby the surface sensitivity could be significantly increased.

Further on, the total scattering cross sections of water vapour were measured in unprecedented accuracy using a commonly known beam current measurement technique in combination with the ESEM improvements.

Finally, the ESEM purging sequence was significantly improved in order to minimize sample evaporation during pumpdown and an optimized purging procedure without technical changes to the microscope was introduced. These new prospects were used to observe liquid and non-liquid biological samples. Human blood cells without any sample preparation and tardigrades were imaged as well as the movement of live mites

at comparatively high chamber pressure.

In any case, it was shown that the field of applications of commercially available ESEMs such as the FEI Quanta line ESEM can be widely extended by modifying the microscope's SE detection as well as the pressure limiting system.

Bibliography

- Cameron, R.E., & Donald, A.M. 1994. Minimizing sample evaporation in the environmental scanning electron microscope. *Journal of Microscopy*, **173**(3), 227–237.
- Danilatos, G.D. 1983. A gaseous detector device for an environmental SEM. *Micron and microscopica acta*, **14**(4), 307–318.
- Danilatos, G.D. 1988. Foundations of Environmental Scanning Electron Microscopy. *Pages 109 – 250 of:* Hawkes, Peter W. (ed), *Advances in Electronics and Electron Physics*. Advances in Electronics and Electron Physics, vol. 71. Academic Press.
- Danilatos, G.D. 1990a. Equations of charge distribution in the environmental scanning electron microscope (ESEM). *Scanning microscopy*, **4**(4), 799–823.
- Danilatos, G.D. 1990b. Theory of the Gaseous Detector Device in the Environmental Scanning Electron Microscope. *Advances in Electronics and Electron Physics*, vol. 78. Academic Press.
- Danilatos, G.D. 2009. Optimum beam transfer in the environmental scanning electron microscope. *Journal of Microscopy*, **234**(1), 26–37.
- Danilatos, G.D. 2013a. Electron scattering cross-section measurements in ESEM. *Micron*, **45**, 1 – 16.
- Danilatos, G.D. 2013b. Implications of the figure of merit in environmental SEM. *Micron*, **44**, 143 – 149.
- Danilatos, G.D., & Robinson, V.N.E. 1979. Principles of scanning electron microscopy at high specimen chamber pressures. *Scanning*, **2**(2), 72–82.

- Danilatos, G.D., Matthew, P.R., & Nailon, J.V. 2000. Electron beam loss in commercial ESEM. *16th Australian conference on electron microscopy*, **1970**, abstracts: 81–82.
- Danilatos, G.D., Rattenberger, J., & Dracopoulos, V. 2011. Beam transfer characteristics of a commercial environmental SEM and a low vacuum SEM. *Journal of Microscopy*, **242**(2), 166–180.
- Dean, C. 2015. *The Tardigrade: Practically Invisible, Indestructible ‘Water Bears’*. New York Times. Retrieved from <http://www.nytimes.com/2015/09/08/science/the-tardigrade-water-bear.html> on 2017-01-04.
- Dortmund Data Bank. 2017. *Saturated Vapor Pressure*. Retrieved from <http://ddbonline.ddbst.de/AntoineCalculation/AntoineCalculationCGI.exe> on 2017-01-17.
- Egerton, R.F., Li, P., & Malac, M. 2004. Radiation damage in the TEM and SEM. *Micron*, **35**(6), 399 – 409. International Wuhan Symposium on Advanced Electron Microscopy.
- Fitzek, H. 2014. *Optimizing the Environmental Scanning Electron Microscope for chamber pressures up to 2700 Pa*. M.Phil. thesis, Graz University of Technology, Austria.
- Fitzek, H., Schröttner, H., Wagner, J., Hofer, F., & Rattenberger, J. 2015. Experimental evaluation of environmental scanning electron microscopes at high chamber pressure. *Journal of Microscopy*, **260**(2), 133–139.
- Fitzek, H., Schröttner, H., Wagner, J., Hofer, F., & Rattenberger, J. 2016. High-quality imaging in environmental scanning electron microscopy - optimizing the pressure limiting system and the secondary electron detection of a commercially available ESEM. *Journal of Microscopy*, **262**(1), 85–91.
- Gauvin, R. 1999. Some theoretical considerations on X-ray microanalysis in the environmental or variable pressure scanning electron microscope. *Scanning*, **21**(6), 388–393.
- Goldstein, J.I., Lyman, C.E., Newbury, D.E., Lifshin, E., Echlin, P., Sawyer, L., Joy,

- D., & Michael, J. 2003. *Scanning Electron Microscopy and X-Ray Microanalysis*. 3 edn. Springer.
- Lane, W.C. 1970. The environmental control stage. *Scanning Electron Microscopy*, **1970**, 43–48.
- Miller, W. 2011 (September-October). *Tardigrades*. American Scientist. Retrieved from <http://www.americanscientist.org/issues/pub/2011/5/tardigrades/1> on 2017-01-09.
- Nasser, E. 1971. *Fundamentals of Gaseous Ionization and Plasma Electronics (Wiley series in plasma physics)*. John Wiley & Sons Inc.
- Philips Electron Optics. 1996. *Environmental Scanning Electron Microscopy, An Introduction to ESEM[®]*. 2nd printing. El Dorado Hills: Robert Johnson Associates.
- Rattenberger, J., Wagner, J., Schröttner, H., Mitsche, S., Schaffer, M., & Zankel, A. 2008. *Experimental determination of the total scattering cross section of water vapour and of the effective beam gas path length in a low vacuum scanning electron microscope*. Berlin, Heidelberg: Springer Berlin Heidelberg. Pages 601–602.
- Rattenberger, J., Wagner, J., Schröttner, H., Mitsche, S., & Zankel, A. 2009. A method to measure the total scattering cross section and effective beam gas path length in a low-vacuum SEM. *Scanning*, **31**(3), 107–113.
- Rattenberger, J., Fitzek, H., Schröttner, H., & Wagner, J. 2014. *Elektronenmikroskop und Verfahren zum Untersuchen einer Probe mit dem Elektronenmikroskop*. Patent pending: A50897, Austria.
- Robinson, V.N.E. 1975. A wet stage modification to a scanning electron microscope. *Journal of Microscopy*, **103**(1), 71–77.
- Sergwyn, S. 2015 (April 6). *New discovery. meet Tardigrades the Seabear*. Retrieved from <http://nafasocietyandmedia.blogspot.co.at/2015/04/new-discovery-meet-tardigrades-seabear.html> on 2017-01-09.

- Shah, J.S., & Becket, A. 1979. A preliminary evaluation of moist environment ambient temperature scanning electron microscopy. *Micron (1969)*, **10**, 13–23.
- Spivak, G.V., Rau, E.I., Karelin, N.M., & Mishustina, I.E. 1977. Scanning electron microscopy of moist, live, and frozen objects. *Akad. Nauk SSSR, Ser. Fiz.* **41**, 11:2238–2251 (Russian).
- Stokes, D. 2008. *Principles and Practice of Variable Pressure/Environmental Scanning Electron Microscopy (VP-ESEM)*. RMS - Royal Microscopical Society. Wiley.
- Thiel, B.L., Bache, I.C., Fletcher, A.L., Meredith, P., & Donald, A.M. 1997. An improved model for gaseous amplification in the environmental SEM. *Journal of Microscopy*, **187**(3).
- Tihlaříková, E., Neděla, V., & Shiojiri, M. 2013. In Situ Study of Live Specimens in an Environmental Scanning Electron Microscope. *Microscopy and Microanalysis*, **19**(4), 914–918.
- Ulbricht, M., Schuster, O., Ansorge, W., Ruetering, M., & Steiger, P. 2007. Influence of the strongly anisotropic cross-section morphology of a novel polyethersulfone microfiltration membrane on filtration performance. *Separation and Purification Technology*, **57**(1), 63 – 73.
- von Engel, A. 1965. *Ionized Gases*. 2 edn. Oxford University Press.

List of Figures

2.1	Schematic representation of the vacuum system of an ESEM. The vacuum system is divided into five stages with increasing vacuum from the bottom to the top level. The different stages are separated by pressure limiting apertures (PLAs). (Philips Electron Optics, 1996)	5
2.2	Enlarged pole piece from figure 2.1 showing two pressure limiting apertures (PLAs) which maintain high vacuum conditions in the electron column while there is comparatively high pressure in the sample chamber. (Philips Electron Optics, 1996)	6
2.3	The average number of scattering events per electron m determines the scattering regimes. CSEMs operate in the minimal scattering regime, whereas ESEMs operate in the partial scattering regime. The complete scattering regime cannot be used for SEM imaging. (Philips Electron Optics, 1996)	7
2.4	The positively biased gaseous secondary electron detector accelerates secondary electrons which in turn ionize gas atoms or molecules. The electrons coming from the ionization process themselves ionize further gas atoms and the result is an electron cascade, which is collected by the GSED. (Philips Electron Optics, 1996)	10
2.5	Schematic drawing of the pressure limiting system of the FEI Quanta line ESEMs. Image provided by FELMI-ZFE.	11

2.6	Schematic drawing of the improved pressure limiting system including the experimental secondary electron detector (ESED). Image provided by FELMI-ZFE.	12
2.7	Vapour pressure diagram of water calculated by Antoine equation. By variation of pressure or temperature, the sample can be hydrated, evaporated or any hydration state can be maintained. Calculation parameters taken from Dortmund Data Bank (2017).	13
3.1	Design of a sample according to Fitzek (2014) (a) : approximately 12 μm copper wire put on carbon tape. Due to the cylindrical shape of the copper wire, clear differences in brightness can be seen on the right side. Improved design of sample (b) used for the SNR measurement in this work: copper block embedded in CaldoFix. Highly polished finally with diamond suspension down to 0.1 μm grain size.	16
3.2	Average mean gray value (from 0 = black to 255 = white) of all lines from original sample compared to improved sample.	17
3.3	Error estimation of the used algorithm: SNR of 10 ESEM images using the GSED acquired under the same conditions (water vapour environment, pressure of 250 Pa, fixed WD of 10.0 mm, accelerating voltage of 20.0 kV and a beam current of 1.0 nA) calculated by the algorithm of Fitzek (2014).	18
3.4	SNR as a function of the ED measured for different pressures at an accelerating voltage of 30.0 kV and a beam current of 1.0 nA.	19
3.5	SNR as a function of the ED measured for different pressures at an accelerating voltage of 20.0 kV and a beam current of 1.0 nA.	19
3.6	SNR as a function of the ED measured for different pressures at an accelerating voltage of 15.0 kV and a beam current of 1.0 nA.	20
3.7	SNR as a function of the ED measured for different pressures at an accelerating voltage of 10.0 kV and a beam current of 1.0 nA.	20

3.8	SNR as a function of the ED measured for different pressures at an accelerating voltage of 5.0 kV and a beam current of 1.0 nA.	21
3.9	SNR as a function of the ED measured for different pressures at an accelerating voltage of 3.0 kV and a beam current of 1.0 nA.	21
3.10	Optimized working distance WD_{opt} as a function of pressure for different accelerating voltages.	23
4.1	MicroPES [®] 2F membrane analysed with GSED. Pixel dimension: 1024x884; Dwell time: 1 μ sec; Frame time: 0.97 sec.	27
4.2	Performance of GSED in combination with original aperture holder at PE beam energies of 7.0 keV (a) , 5.0 keV (b) and 3.0 keV (c) . Image quality is strongly dependent on PE beam energy and very poor for low energies. Pixel dimension: 1024x884; Dwell time: 0.5 μ sec; Frame time: 0.49 sec.	27
4.3	Positioning of ESED (tungsten needle tip) above sample. Teflon holder (a) (white) attached to the Peltier stage. The position and height of the needle can be adjusted using the screws. Position of needle tip (b) in direct proximity to the sample surface.	28
4.4	Performance of ESED (tungsten needle tip fixed on sample table) in combination with modified aperture holder (final PLA diameter of 200 μ m) at PE beam energy of 7.0 keV (a) , 5.0 keV (b) and 3.0 keV (c) . Image quality remains sufficiently well, even at low PE beam energies. Pixel dimension: 1024x884; Dwell time: 0.5 μ sec; Frame time: 0.49 sec.	29
4.5	Wetting experiment with PE beam energy of 5.0 keV at 800 Pa. Membrane pores are continuously filled with water during cooling from 2.9 $^{\circ}$ C with a cooling rate of 0.2 $^{\circ}$ C/min. Pixel dimension: 1024x884; Dwell time: 10 μ sec; Frame time: 9.48 sec.	30

4.6	Wetting experiment with PE beam energy of 3.0 keV at 800 Pa. Droplet formation on the surface of the membrane during cooling from 4.0 °C with a cooling rate of 0.4 °C/min. Pixel dimension: 1024x884; Dwell time: 10 μsec; Frame time: 9.48 sec.	31
5.1	Elastic, inelastic and total differential cross section for argon at 30 keV electron energy representative for the typical scattering angle distribution of imaging gases in the ESEM. (Rattenberger <i>et al.</i> , 2009)	33
5.2	Schematic drawing of single-shielded Faraday cup. The fraction of PE beam which is unscattered reaches the copper block and can be measured by the ammeter. The scattered fraction of PE beam hits the aluminium foil which is directly grounded over the sample stage of the microscope.	34
5.3	Simple linear fit approach $y = A_U \cdot x$ for measured average number of scattering events per electron as a function of water vapour chamber pressure for different accelerating voltages.	36
5.4	Simple linear fit approach $y = A_U \cdot x + B_U$ for measured average number of scattering events per electron as a function of water vapour chamber pressure for different accelerating voltages. Since all graphs show a positive B_U (zoom square) this might give a sign for a small remaining systematic error of the measurement.	38
6.1	FEI Quanta 600 FEG ESEM [®] settings offer three purging options.	42
6.2	Vapour pressure of water as a function of temperature calculated by Antoine equation. The line represents 100% RH where the evaporation rate equals to the condensation rate and there is no net loss or gain of water. The red dot marks the point where the experiments were performed ($T = (6.5 \pm 0.3)$ °C and $p = 970$ Pa). Calculation parameters taken from Dortmund Data Bank (2017).	44

6.3	Scheme of FEI ‘auto purging’ sequence: pumpdown from atmospheric pressure to 130 Pa, flooding the sample chamber with water vapour up to 1300 Pa, repeating this cycle one more time and afterwards final pumpdown to the desired pressure.	45
6.4	FEI Quanta 600 FEG ESEM [®] ‘auto purging’ experiment: The droplets (liquid sample) are clearly visible in the beginning (a) . After the first pumpdown to 130 Pa (b) the droplets are evaporated. Until the purging sequence is completed and the imaging conditions are reached (c) condensation can be observed but the initial droplets have completely vanished.	45
6.5	FEI Quanta 600 FEG ESEM [®] ‘no purging’ experiment: The droplet (liquid sample) is clearly visible in the beginning (a) . During direct pumpdown to the desired imaging pressure (b) the droplet loses mass. Until the imaging pressure is reached (c) the droplet has completely vanished and no condensation on the surface is visible.	46
6.6	Scheme of tested ‘custom purging’ sequence according to parameters from Cameron & Donald (1994): pumpdown from atmospheric pressure to desired imaging pressure, flooding the sample chamber with water vapour up to imaging pressure + 500 Pa, repeating this cycle eight times and afterwards again pumpdown to the desired imaging pressure.	47
6.7	FEI Quanta 600 FEG ESEM [®] ‘custom purging’ experiment: The droplets (liquid sample) are clearly visible in the beginning (a) . After the first pumpdown to the desired imaging pressure (970 Pa) the droplets have lost a small amount of mass. Until the purging sequence is repeated eight times and the imaging pressure is reached (c) , the initial droplets are kept hydrated with low mass loss. Condensation on the surface is observable after the first cycle.	47

6.8	FEI Quanta 600 FEG ESEM [®] ‘improved custom purging’ experiment (additional spongiouse water reservoir in sample chamber): The droplets (liquid sample) are clearly visible in the beginning (a) . After the first pumpdown to the desired imaging pressure (970 Pa) the droplets have almost the same mass. Until the purging sequence is repeated eight times and the imaging pressure is finally reached (c) , the initial droplets are kept hydrated without significant mass loss. Condensation on the surface is observable after the first cycle and clearly visible at the end. .	49
6.9	Tardigrade’s active and resilient tun state. In the tun state the tardigrade can withstand extreme conditions. (Sergwyn, 2015)	50
6.10	Hydration process of tardigrade. The typical tun state (a) starts to get hydrated slightly (b) . Further hydration (c) finally leads to the typical shape of the active (hydrated) state (d) . Hydration by cooling from 4 °C to 2 °C at 800 Pa water vapour. Pixel dimension: 1024x884; Dwell time: 10 μ sec; Frame time: 9.47 sec.	52
6.11	SEM image of human blood cells. Sample preparation efforts: glutaraldehyde fixation, osmium tetroxide postfixation, dehydration in an ascending alcohol series and gold sputtering. Preparation and image acquisition by Claudia Mayrhofer (FELMI-ZFE).	53
6.12	ESEM image of human erythrocyte without any considerable sample preparation efforts acquired in ESEM at 1500 Pa using needle tip ESED and 200 μm final PLA. Pixel dimension: 1024x884; Dwell time: 1 μ sec; Frame time: 0.95 sec.	54

-
- 6.13 Observation of a live mite (*oribatida*) in ESEM at comparatively high pressure. Images selected from video movement documentation. The movement of the limbs (red arrows) is clearly visible whilst the mite is in supine position at water vapour pressure of 2200 Pa and room temperature using needle tip ESED and a 400 μm final PLA. Due to the size of the animal, only the front body part is shown in these images. The diagonal stripes in the picture are not explained yet and might be caused by insufficient grounding of the microscope or electronic disturbances. Pixel dimension: 512x442; Dwell time: 3 μsec ; Frame time: 0.76 sec. 55

List of Tables

3.1	Results of measurement for optimized working distance WD_{opt} for different pressures and accelerating voltages. The values give the range where the maximum SNR was measured within the experimental and systematic error of the method.	24
5.1	Fit results for measured data points shown in figure 5.3 fitted by a simple linear regression $y = A_U \cdot x$	37
5.2	Total scattering cross sections for water vapour calculated from simple linear fit parameters in table 5.1.	38
5.3	Measured total scattering cross sections for water vapour from table 5.2 compared to those from Rattenberger <i>et al.</i> (2009) and also compared to theoretical calculations from Danilatos (2013a).	39

List of Abbreviations

BSE	backscattered electron
CSEM	conventional high vacuum scanning electron microscope
ED	environmental distance
ESED	experimental secondary electron detector
ESEM	environmental scanning electron microscope
ETD	Everhart-Thornley detector
FEG	field emission gun
FEI	Field Electron and Ion Co. (company name)
FELMI-ZFE	Institute of Electron Microscopy and Graz Centre for Electron Microscopy (institute's name)
FIB	focused ion beam
GSED	gaseous secondary electron detector
LFD	large field detector
LV-SEM	low-vacuum scanning electron microscope
PE	primary electron(s)
PLA	pressure limiting aperture
RH	relative humidity
SE	secondary electron
SEM	scanning electron microscope
SNR	signal-to-noise ratio
WD	working distance